JGR Oceans

RESEARCH ARTICLE
10.1029/2021JC017290

The Nature of Ice Intermittently Accreted at the Base of Ronne Ice Shelf, Antarctica, Assessed Using Phase-Sensitive Radar

Irena Vaňková[1], Keith W. Nicholls[1], and Hugh F. J. Corr[1]

[1]British Antarctic Survey, Natural Environment Research Council, Cambridge, UK

Key Points:

- Intermittent accretion at three sites that are melting in the long-term mean is detected and quantified using phase-sensitive radar (ApRES)
- Episodic basal accretion along the western Ronne Ice Shelf is caused by frazil ice deposition
- ApRES can be used to study the evolution of boundaries between basal melting and basal accretion regimes

Supporting Information:

Supporting Information may be found in the online version of this article.

Correspondence to:

I. Vaňková,
irkova@bas.ac.uk

Citation:

Vaňková, I., Nicholls, K. W., & Corr, H. F. J. (2021). The nature of ice intermittently accreted at the base of Ronne Ice Shelf, Antarctica, assessed using phase-sensitive radar. *Journal of Geophysical Research: Oceans*, *126*, e2021JC017290. https://doi.org/10.1029/2021JC017290

Received 18 FEB 2021
Accepted 20 SEP 2021

Abstract In-situ phase-sensitive radar measurements from the Ronne Ice Shelf (RIS) reveal evidence of intermittent basal accretion periods at several sites that are melting in the long-term mean. Periods when ice is accreted at the ice-shelf base coincide with a decrease in the amplitude of the basal return of up to 4 dB. To quantify basal accretion we constrain simultaneously the dielectric constant, electrical conductivity, and thickness of the accreted ice. We do this by exploring the sensitivity of the received basal echo strength and phase to different transmit frequencies using the radar data in combination with a simple model. Along the western RIS, we detect episodic basal accretion events leading to ice accumulation at a rate equivalent to 1–3 mm of meteoric ice per day. The inferred accumulation rates and electromagnetic properties of the accreted ice imply that these events are caused primarily by the deposition of frazil ice crystals. Our findings offer the possibility of monitoring and studying the evolution of boundaries between ice-shelf basal melting and accretion regimes using remote observations, collected from the ice-shelf surface.

Plain Language Summary Ice shelves, the floating portions of the Antarctic Ice Sheet, interact with the ocean beneath, resulting in melting or freezing at the ice-shelf base. As the access to the ocean beneath the ice shelf is difficult and costly, techniques that can measure changes at the ice base remotely, such as ground-based radar, offer a desirable alternative to observing ice-ocean interactions directly. A phase-sensitive radar can precisely measure the evolution of the rate at which ice shelves melt at their base by detecting changes in the phase of the reflected signal. However, using this technique to detect and quantify the rate of basal accretion is complicated by the fact that the electromagnetic properties of the frozen-on ice, key to quantifying its thickness, are unknown. We detected intermittent accretion periods at several ice-shelf locations by investigating changes in the strength of the radar signal returned from the ice base. Furthermore, we developed a method that can simultaneously quantify the thickness and the electromagnetic properties of the accreted ice. This new observational capability expands the range of ice-ocean interaction regimes that can be monitored from the ice-shelf surface.

1. Introduction

As the Antarctic Ice Sheet flows under its own weight it thins toward its edges and when meeting the surrounding ocean it often goes afloat to form ice shelves. The floating ice shelves matter to the flow of the grounded ice because they buttress it, and they matter to the ocean because in the ocean cavities beneath they transform water masses by melt-freeze interactions at the ice-ocean boundary. Thick and cold ice shelves such as the Filchner-Ronne Ice Shelf (FRIS), where the warmest water mass that comes into contact with their base is at the surface freezing point (~−1.9 °C), contribute to defining the properties of the deepest and coldest waters of the world's oceans (Foldvik et al., 1985). The warmest water mass reaching the majority of the base of FRIS is the high-salinity shelf water (HSSW) formed by the freezing of sea ice at the ocean surface above the continental shelf. By interactions with the ice shelf, HSSW is transformed into ice-shelf water (ISW) that is colder and fresher (Gammelsrød et al., 1994). As the buoyant ISW rises along the sloped ice-shelf base, its pressure reduces, increasing the in-situ freezing temperature such that it may become in-situ supercooled (Lewis & Perkin, 1986). Supercooling is relieved by the crystallization of frazil ice within the water column. The crystals then grow in size and precipitate at the ice-shelf base, eventually consolidating and forming marine ice. For FRIS, marine ice constitutes over 5% of its volume and it can be several hundreds of meters thick (Lambrecht et al., 2007; Oerter et al., 1992).

The processes by which frazil ice grows into platelets that consolidate to form a marine-ice layer that is bubble-free, more saline, and crystallographically different to glacial ice of meteoric origin can be inferred from ice cores (Craven et al., 2009; Oerter et al., 1992). However, direct in-situ observations of the process of freezing and basal accretion beneath ice shelves are challenging as the instrumentation disrupts the supercooled environment it attempts to observe and the icing-up of sensors corrupts the measurements (N. J. Robinson et al., 2020). At times transitions between basal melting and accretion regimes beneath an ice shelf have been observed indirectly in surprising ways. For example, Craven et al. (2014) inferred transient periods of frazil ice formation beneath Amery Ice Shelf from changing pressure readings of moored instruments that occasionally became sufficiently coated with platelets that the change in buoyancy caused them to rise. Evidence of relatively recently ceased basal accretion has been gathered from the central Ross Ice Shelf, where a camera descended to the ice-shelf base through a borehole recorded imagery featuring a 10-cm layer of crystals, despite weakly melting conditions (Stevens et al., 2020).

More systematic indirect observations of the basal accretion process, such as by using a ground-based radar are complicated by various factors. First, even consolidated marine ice is significantly saltier, and therefore more conductive than glacial ice, and its absorption of radar wave energy is an order of magnitude higher. Consequently, for a sufficiently thick marine-ice layer the reflection from an ice-ocean interface may not be detectable (Corr et al., 2002; Morey & Kovacs, 1982; Thyssen, 1988). Second, knowledge of the electromagnetic properties is necessary to make quantitative estimates of radar-derived ice thickness evolution. However, the electromagnetic properties of the accreted ice formed from ISW will depend on its consolidation and salinity; factors that can change through time. Third, the basal roughness may change as the ice base goes from melting to accretion (Neal, 1979; Robin et al., 1983), or as frazil ice deposits non-uniformly at the ice base. If at a length scale similar to, or greater than, the radar wavelength, interfacial roughness can cause changes in the perceived properties of the basal reflection and result in uncertainty in ice thickness change estimates.

The recent development of the autonomous phase-sensitive radio-echo sounder, (ApRES; Brennan et al., 2014; Nicholls et al., 2015), has enabled precise observations of basal melt rate evolution at timescales as short as days to weeks by detecting small changes in the phase of the reflected signal. While the concerns regarding the feasibility of ice base detection and the interpretation of an accretion signal remain for the case of regions that experience such conditions in the long term mean, the situation may be different for sites that melt on average but experience intermittent accretion. This is because, in addition to the detecting phase, ApRES is a wide-band radar; both of these characteristics increase the amount of measured information about the character of potential changes taking place at the ice-shelf base. The transitions between the presence and absence of accreted ice are essential, as they provide a clear change in regime that should be reliably identifiable. The aim of this paper is to characterize intermittent anomalies in the basal echo in the ApRES time series obtained from three sites on Ronne Ice Shelf (RIS). We will show that these anomalies are caused by episodic basal accretion and we will constrain the properties of the accreted ice using the multitude of information contained in the ApRES signal.

The remainder of the paper is structured as follows. Section 2 introduces the data and provides a background on the ApRES technique. Section 3 presents observations of the characteristics of basal echo anomalies, identifying two distinct regimes depending on the presence/absence of accreted ice, and it explores the dependence of the return amplitude and phase change on the radar's center frequency in the case when accreted ice is present. Section 4 describes a simple three-layer model that allows the accreted thickness and electromagnetic properties to be constrained simultaneously, using the observable quantities and their variation across a range of radar frequencies. Section 5 focuses on the analysis of data from individual sites. Section 6 discusses the results in terms of the accretion mechanisms that could give rise to the inferred accreted ice thickness and properties. Section 7 highlights how the capability to detect basal accretion impacts other applications of the ApRES technique: the mean strain rate estimation and the estimation of mean melt rate from infrequent measurements. Section 8 summarizes our conclusions.

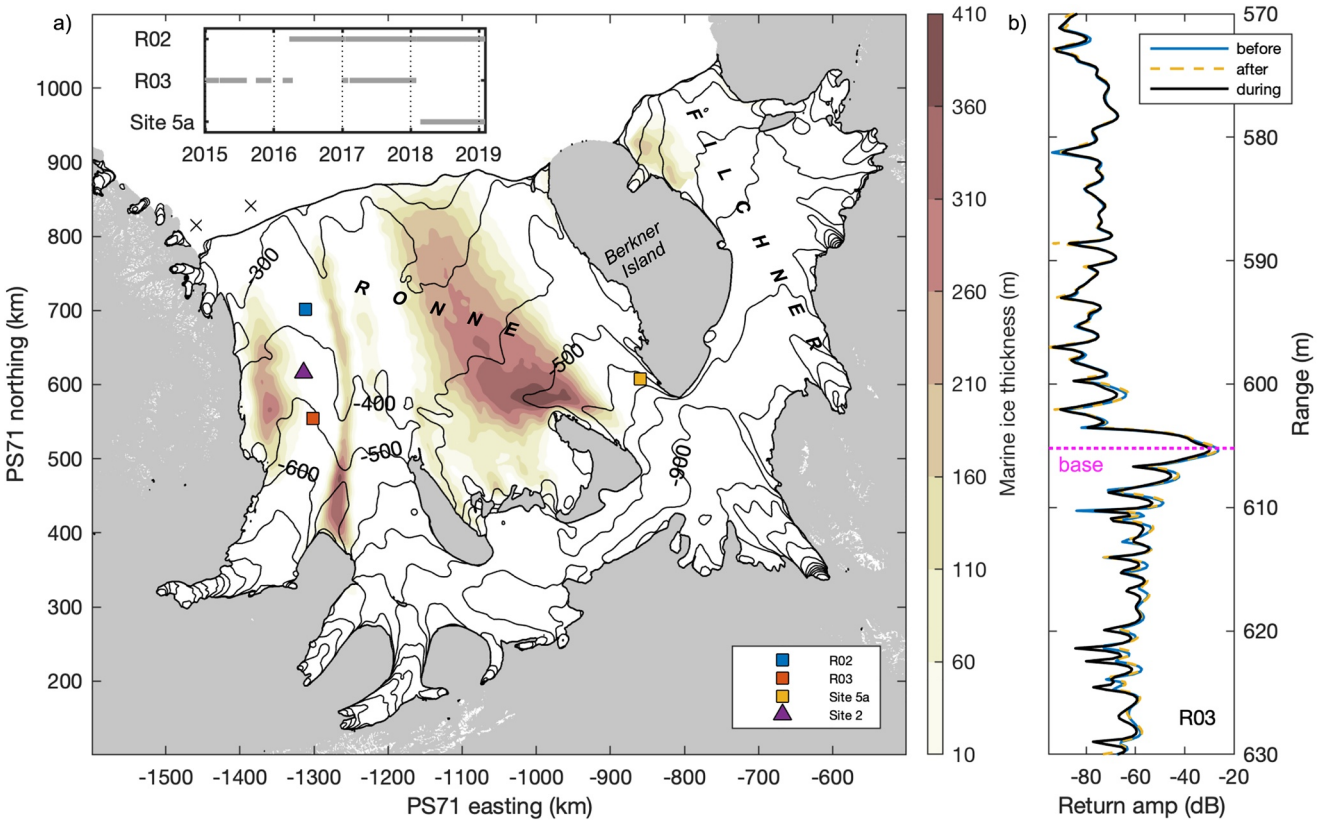

Figure 1. (a) Map of the study area. R02, R03, and Site 5a are ApRES occupied sites, where intermittent accretion was detected. Oceanographic observations at Site 2, collected in the 1990s through a borehole, showed evidence of frazil ice presence in the upper part of the water column. The labeled line contour shows ice draft at 100 m spacing from Morlighem et al. (2020) and the filled contour marine-ice thickness at 50 m spacing from Lambrecht et al. (2007). R02, R03, and Site 2 are located on the eastern flank of the Ronne Depression, a bathymetric feature beneath the western most portion of the cavity. The inset shows periods analyzed for basal accretion at each ApRES site. Two black crosses along the western ice front mark locations where past moorings detected outflows of ice shelf water. (b) Example amplitude returns from site R03 from before, after, and during an accreted-ice event show that the amplitude of basal returns (at ranges greater than ~600 m) is lower during the event, while for internal ice reflectors (at ranges shorter than ~600 m) the return amplitude remains constant. The ice-shelf thickness is given by the location of the largest peak at ~605 m (dashed magenta line); an earlier smaller peak at ~601 m range results from spectral leakage and it carries the same temporal characteristics as the main basal peak.

2. Data and Methods

2.1. Study Site and Data

We present analysis of ApRES data from RIS sites R02, R03, and Site 5a (see Figure 1), that is, locations where we detect anomalies in basal echo, the analysis of which is the subject of this paper. A general description of the full dataset, which includes 17 sites, is provided by Vaňková, Nicholls, Corr, et al. (2020). The study area in Figure 1a shows locations of the three ApRES sites analyzed here and of Site 2, where oceanographic data were collected through a borehole in the 1990s (Nicholls, 1996; A. Robinson et al., 1994). Sites R02 and R03 are located along the western edge of RIS, where the ocean column comprises a deep HSSW inflow overlain by a colder ISW mass (Nicholls et al., 1997). ISW is by definition potentially supercooled, which means that it would become colder than the in-situ freezing point if it were elevated higher in the water column to lower pressure. Site 5a is located near the southwestern coast of Berkner Island. There the water column is composed primarily of ISW although its structure is influenced by several modes of circulation (Nicholls et al., 2001). We analyzed 3 years of ApRES data for R02, 2 years of data for R03, and 1 year of data for Site 5a (see Figure 1a for time periods).

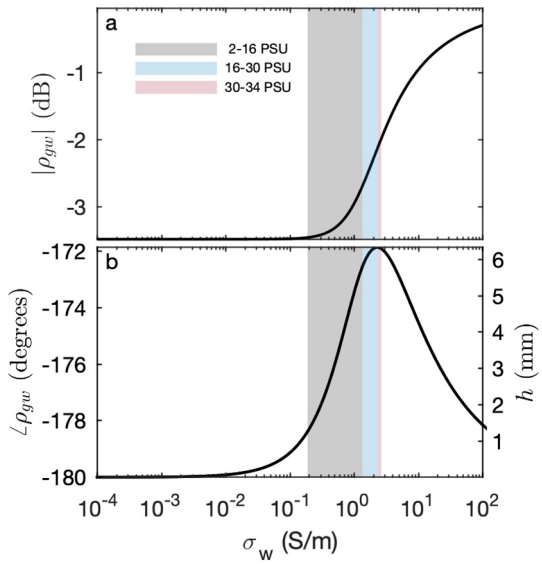

Figure 2. The effect of electrical conductivity of sea water (σ_w) on the reflection from the ice-shelf base for $f_c = 300$ MHz, $\epsilon'_g = 3.18$, $\epsilon'_w = 81$, and $\sigma_g = 10^{-5}$ S/m, where g and w are glacial ice and sea-water properties, respectively. Shaded regions show salinity ranges for RIS-like conditions of 500 m depth and temperature of −2.3°C (a) Amplitude and (b) argument of the complex reflection coefficient; right axis in b shows the corresponding distance scale.

2.2. ApRES Background

The surface-deployed ApRES is a frequency modulated continuous wave system (FMCW) configured to transmit a sequence of 20–30 chirps every 2 hr. Each chirp is a frequency sweep that ramps linearly from 200 to 400 MHz over a 1s period. The received signal is then frequency-deramped by mixing it with the transmitted chirp, and spectrally analyzed, as each frequency f_d contained in a deramped chirp is related to a unique reflector range r (Brennan et al., 2014). The spacing between range bins Δr, that is, the resolution of the radar when used in a phase-insensitive manner, is given by

$$\Delta r = \frac{c}{2B\sqrt{\epsilon'_g}}, \tag{1}$$

where ϵ'_g is the dielectric constant of glacial ice, c the speed of light in vacuum, and B the radar bandwidth. However, ApRES also utilizes the phase of the reflected signal as it is the change in phase between subsequent time shots (averaged sequence of chirps) that provides a precise measurement of a reflector's displacement at much finer resolution than in Equation 1. The temporal changes in the phase of the reflected wave are determined by changes in the reflector range combined with changes in $\angle\rho_{ab}$, the argument of the complex reflection coefficient at normal incidence to the interface separating medium a from medium b, where

$$\rho_{ab} = \hat{\rho}_{ab} S_{ab} = \frac{\eta_b - \eta_a}{\eta_b + \eta_a} S_{ab}. \tag{2}$$

Here, $\hat{\rho}_{ab}$ is the reflection coefficient from a specular reflector and $|S_{ab}| \leq 1$ is a term that includes the effects of the roughness of the ab interface that can depend on a number of parameters (Beckmann & Spizzichino, 1963). Assuming that the permeability is negligible, the impedance η of a medium is calculated as

$$\eta = \frac{1}{\sqrt{\epsilon}}, \tag{3}$$

where $\epsilon = \epsilon' + i\epsilon''$ is the relative permittivity. Its complex part ϵ'' is responsible for dielectric absorption loss and is a function of both the transmit center frequency f_c and of the electrical conductivity σ:

$$\epsilon'' = \frac{\sigma}{2\pi f_c \epsilon_0}, \tag{4}$$

where ϵ_0 is the permittivity of vacuum. σ is highly sensitive to impurities, e.g., salt concentration, and between glacial ice and sea water it varies by five orders of magnitude. In summary, ϵ' and σ of the materials a and b are the properties setting $\hat{\rho}_{ab}$ for a given f_c. However, as we shall detail, for a non-specular reflection it is possible for S_{ab} to be as, or more important for the resulting ρ_{ab}.

For a melting ice shelf, the application for which ApRES was primarily designed, it is assumed that a temporal change in phase stems entirely from a displacement of the basal reflector. This is an approximation because the temporal change in the sea-water conductivity will cause a temporal change in the phase of the reflected signal via η in Equation 2. If the water went from being fresh to salty, the difference in the reflected angle could be up to 8°, which corresponds to over 6 mm for the transmit frequency of 300 MHz (Figure 2). However, under RIS-like conditions, the salinity is near 34 psu and even a relatively large change of 4 psu would result in an apparent thickness change of less than 0.1 mm. Therefore, realistic salinity changes have a negligible effect on phase change on reflection and can be safely omitted.

In this paper, however, we will be concerned with the case of basal accretion, when additional factors have a significant effect on the phase of the reflected signal, and changes in electromagnetic properties ϵ' and σ

at the ice-shelf base mean that it is no longer appropriate to interpret changes in phase solely as changes in ice thickness.

The approach we will use to identify changes in the received basal echo as accreted-ice events (we refer to a time interval over which ice is accreted at the ice base as an accreted-ice event) is based on the analysis of multiple subintervals of the full 1-s chirp. Each chirp subinterval is generated by the transmission of different frequency content (Vaňková, Nicholls, Xie, et al., 2020), with the key variables being center frequency f_c and bandwidth B; for a full chirp, $f_c = 300$ MHz and $B = 200$ MHz. The reason for analyzing multiple chirp subintervals is that both the rate of the signal's attenuation and the phase of the reflected wave received by the ApRES depend on f_c via Equation 4. This f_c dependence provides additional constraints required to accurately interpret the observations of intermittent basal accretion.

The ApRES data were collected using the standard instrument setup, and the analysis that we present here can therefore be directly applied to already existing datasets.

2.3. Time Series

Time series of total ice thickness evolution, excluding surface snow accumulation, were constructed by cross-correlating the complex return signal in a range segment surrounding the basal reflection (Stewart et al., 2019). These displacement time series were filtered with a 2-day low pass filter to remove dominant tidal frequencies and then differentiated to obtain time series of thickness rate of change. The timescales of interest span several days to weeks and we have assumed that the rate at which internal and near-surface thickness changes contribute to the change of total thickness at these timescales are constant. The absence of a significant fortnightly strain rate signal at these sites supports this approach. The internal and near-surface contributions to the measured thickness change were derived from mean vertical profiles of internal layer displacements following Vaňková, Nicholls, Corr, et al. (2020). The final melt rate time series, for the relatively short timescales of interest, is simply the time series of the rate of change of thickness from which the assumed constant internal and near-surface thickness change contributions were subtracted.

We also derive time series of the strength of the signal returned from the ice-shelf base. This is done by tracking the return amplitude of the basal reflector through time. For fixed f_c and B the basal reflection at all three sites is well defined as a sharp peak (e.g., Figure 1b) and its shape is stable through time, allowing a simple tracking of the location of the local maximum. For sites R03 and R02, the shape of the basal reflector are also stable across different f_c, and thus tracking the first strong basal reflection was a suitable approach for obtaining the return amplitude time series at different f_c. The case of Site 5a is different. There the shape of the basal return is sensitive to f_c, the basal reflection has a long tail, and the first peak of the basal return is not always the strongest, nor does it necessarily represent well the amplitude evolution of the remaining off-nadir basal reflectors seen at more distant ranges (Figure S1). Therefore, to obtain more robust temporal changes in the Site 5a basal return, which can be compared for different f_c, we tracked the average basal return amplitude over the first 50 m in range past the first basal reflection. The return-amplitude time series were not low pass filtered at any of the sites.

3. Observations

3.1. Reduction of Basal Return Amplitude During Accreted-Ice Events

Figure 1b shows three shots of return amplitude vertical profiles at R03, separated by 9 days. The return amplitude of the intermediate shot is reduced by ~3 dB compared with earlier and later times at ranges greater than ~600 m, that is, ranges where the ApRES signal is reflected from the ice-shelf base. We discount the cause of the amplitude change being a system artifact because, for internal ice reflectors located above the ice base, the return amplitude remains constant in time. The observation of a temporal change in the strength of the basal reflection shows that the ice-ocean interface properties at R03 evolved over time.

To investigate further the changing nature of the ice base, we track the amplitude of the basal reflector in time and compare its behavior with that of the melt rate time series that were derived from changes in phase. At R02, R03, and Site 5a we observe intermittent periods of decreased return amplitude (Figure 3a) that coincide with instances when ice appears to be accreted at the base (Figure 3b). Time series of apparent

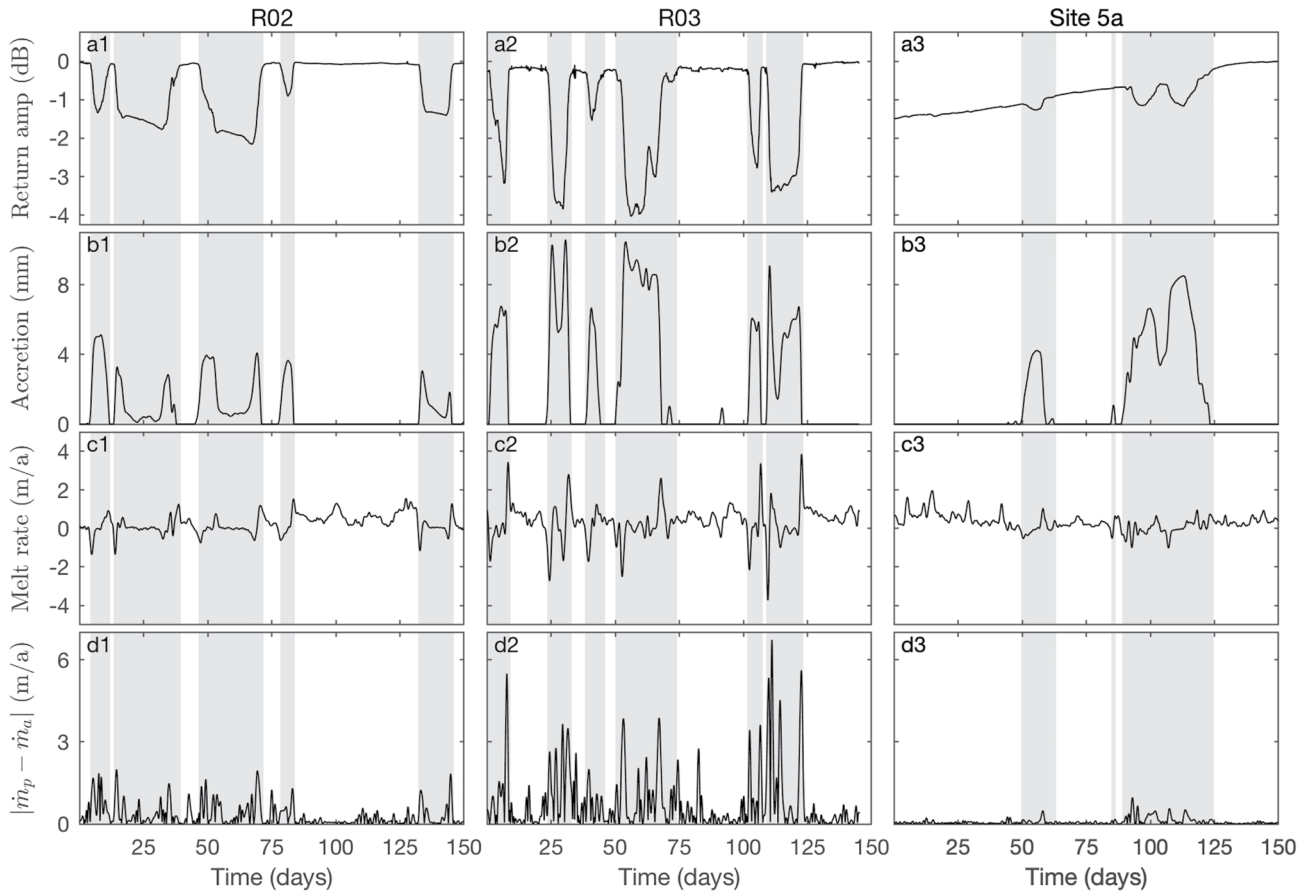

Figure 3. Example time series from the three ApRES sites: (a) Return amplitude, offset to have maximum at 0 dB; (b) Apparent thickness of accreted ice derived from phase; (c) Basal melt rate derived from phase ($\dot{m}_p$); (d) Absolute value of the difference between $\dot{m}_p$ and basal melt rate derived from signal amplitude ($\dot{m}_a$). Shading marks periods during which accreted ice was present at the ice base as determined from the drop in return amplitude.

basal accretion were calculated by integrating the melt rate time series derived by the phase history extracted from the complex correlation of subsequent shots (Figure 3c). Throughout this paper, we use the term apparent accretion for accretion thickness derived by integrating melt-rate time series that uses a dielectric constant of glacial ice to convert phase to displacement in place of the unknown electromagnetic properties of the accreted ice. The actual thickness will differ from the apparent thickness as the contrast between the properties of glacial and accreted ice introduces changes into the phase of the received signal. The variations in the apparent accretion and the return amplitude time series in Figure 3 are remarkably coherent, especially considering that the two quantities rely on two different parts of the radar signal - the former relies heavily on phase while the latter is phase-independent.

3.2. Melt Rate Estimate Sensitivity During Accreted-Ice Events

Because of the aforementioned concerns with using the phase of the signal to measure basal accretion, we seek a complementary phase-independent estimate of accretion. One alternative method is to track the range of the peak of the basal return amplitude to obtain a phase-independent estimate of the total thickness evolution. However, this method is sensitive to small changes in the shape of the basal return, in which case the resulting time series will appear noisy. Figure 3d shows the difference in melt rates derived using the two methods ($\dot{m}_p$ is the melt rate derived using complex cross-correlation that relies on phase and $\dot{m}_a$ is the melt rate derived using amplitude tracking). For all three sites $|\dot{m}_p - \dot{m}_a|$ is significantly lower in the absence of accreted ice. However, when accreted ice is present, $|\dot{m}_p - \dot{m}_a|$ becomes high. Although its

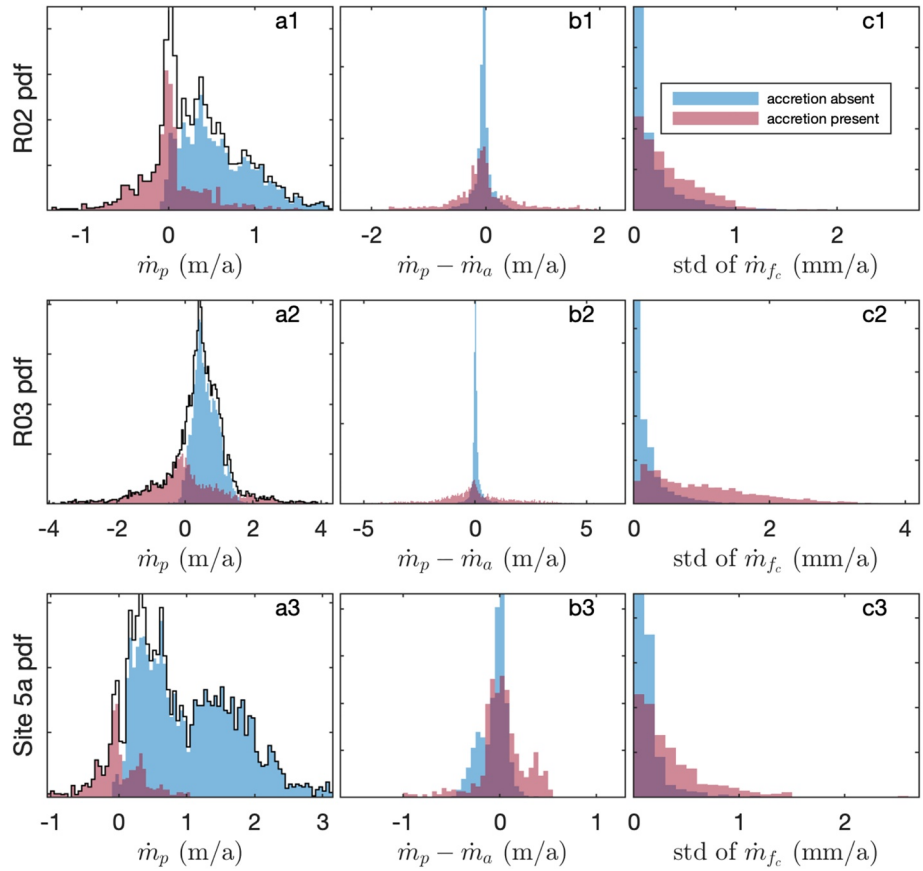

Figure 4. Dependence of the inferred melt rate distribution and properties on the presence of accreted ice. (a) Melt rate distribution (black contour) derived using signal phase ($\dot{m}_p$), the two colored partitions are created based on the presence or absence of accreted ice. (b) Difference between $\dot{m}_p$ and melt rate derived by tracking signal amplitude ($\dot{m}_a$). (c) Std dev. of melt rate derived using a range of center frequencies as in Figure 6. For better comparison, each distribution in b and c has been normalized.

sensitivity to small changes in the shape of the basal reflection makes $\dot{m}_a$ less reliable, it provides the first piece of evidence that the non-thickness related phase changes can be significant.

Histograms in Figure 4 summarize how $\dot{m}_p$, $\dot{m}_a$, and their difference depend on the presence of accreted ice. Figure 4a shows the $\dot{m}_p$ distribution for events with and without accreted ice for the three sites. At R02 an accreted-ice event is characterized by a high accretion rate at the beginning of the event and a high melt rate at its termination (Figure 3c). During the intermediate time, the melt rate stays near zero and it has less variability than during times with no apparent accretion, as shown by the pronounced peak in the distribution near zero in Figure 4a. At R03 the range of melt rates observed during the accreted state is four times as large as in the absence of apparent accretion (Figure 4a). At Site 5a the differences between the two states are less clear, possibly because the number of accreted-ice events is too small to show consistent and distinct statistics (Figure 4a). Figure 4b shows $\dot{m}_p - \dot{m}_a$, indicating that the differences between the two methods are consistently larger during accreted-ice events for all three sites. Finally, Figure 4c shows that the standard deviation of melt rates derived using a range of different f_c (see Section 3.3) is consistently higher in the presence of accreted basal ice for all sites.

3.3. Accretion and Amplitude Dependence on Transmit Center Frequency

The characteristics of the reflection from the ice-shelf base depend on f_c via Equations 1–4. If either the material in contact with the base or the basal roughness were to change, so would the amplitude and phase of the reflected wave in line with Equation 2. If the signal phase alone were used to determine the displacement

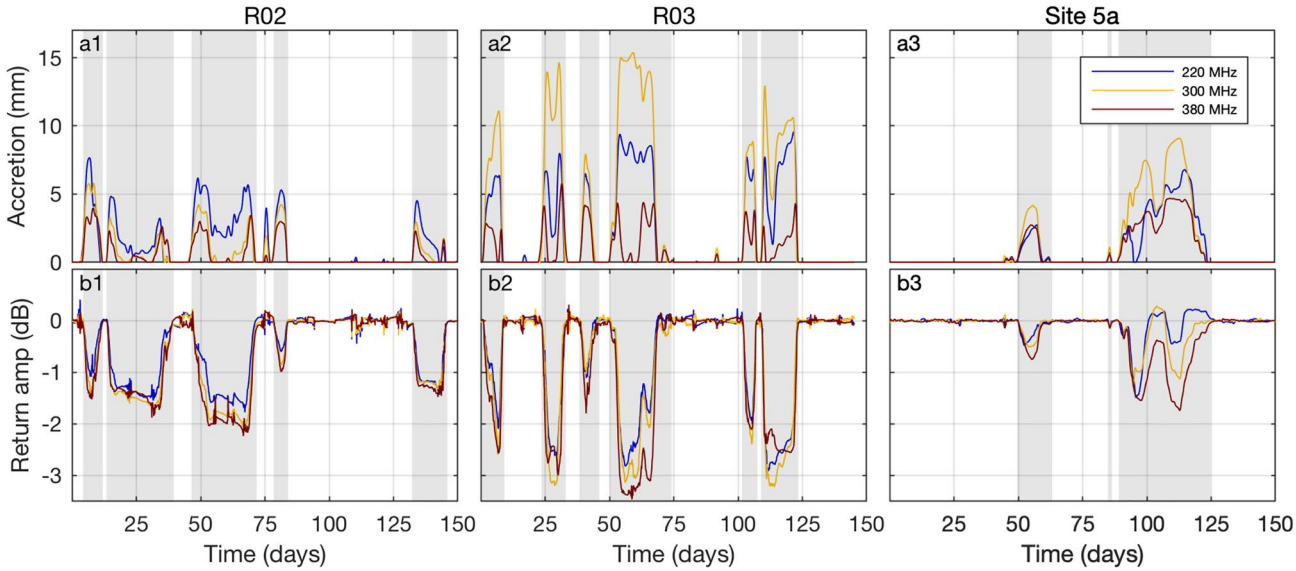

Figure 5. Dependence of apparent accretion and return-amplitude drop on center frequency (f_c). Example time series from the three sites were generated using different subsets of the deramped chirp, corresponding to f_c of 220, 300, and 380 MHz while bandwidth was kept constant at 40 MHz. The underlying trend was removed from the return amplitude time series in b1-b3. Shading marks approximate time periods during which accreted ice was present at the ice base.

of the basal reflector, any such phase shift could be interpreted as motion of the ice base. Therefore, we investigate whether the derived apparent accretion and return amplitude reduction are sensitive to f_c. We fix $B = 40$ MHz as this choice provides good range of f_c that we can explore while still allowing us to focus on the basal reflector with adequate range resolution. Next, the processing steps from Section 2.3 are repeated to obtain basal return amplitude and apparent accretion time series for a range of different f_c. Figure 5 shows the same examples as Figure 3, but now the time series were obtained using $B = 40$ MHz and three different f_c settings: 220, 300, and 380 MHz. For all three sites both the size of the return-amplitude drop and the accreted ice thickness depend on f_c. The f_c dependence is particularly strong for apparent accretion but it is not the same across different sites. For example, R02 has the largest apparent accretion for the lowest of the three f_c settings, while for R03 and Site 5a the apparent accretion is highest for the intermediate f_c setting. While f_c affects the apparent accretion and the amplitude drop, it does not influence the duration of the accreted-ice event, which we define by the duration of the amplitude drop. This means that although we are unsure of the actual accreted ice thickness, the duration over which electromagnetic properties at the ice base changed due to the presence of the accreted-ice layer is unambiguous.

Figure 6 shows the results of a systematic investigation of the f_c dependence of apparent accretion and basal return-amplitude drop for all detected accreted-ice events at each site. We keep B at 40 MHz and vary f_c from 220 to 380 MHz. Then for each event we extract the amplitude drop (ΔR_{obs}) and apparent accretion (Δh_{obs}) at a time when the amplitude drop has reached its maximum.

For R02, we detected eight accreted-ice events lasting between 6 and 35 days (Figure 6a). ΔR_{obs} associated with these events increases with increasing f_c from −1.5 dB at 220 MHz to −2 dB at 380 MHz, and Δh_{obs} decreases with increasing f_c from 6.5 mm at 220 MHz to 3.5 mm at 380 MHz on average.

For R03, there were 39 accreted-ice events recorded (Figure 6b). There is a high number of shorter events, lasting less than five days, however, longer events last as much as 23 days. Both ΔR_{obs} and Δh_{obs} sharply increase with event duration up until 5–7 days before converging to a different value for each f_c. For this site the ΔR_{obs} and Δh_{obs} dependence on f_c is not monotonic. There is a pronounced local minimum in ΔR_{obs} of −4 dB at 280 MHz and a local Δh_{obs} maximum of 12 mm at 300 MHz. Over the range of available f_c and for events lasting longer than 5 days, ΔR_{obs} converges to values between −2 and −4.5 dB and Δh_{obs} between 4 and 12 mm.

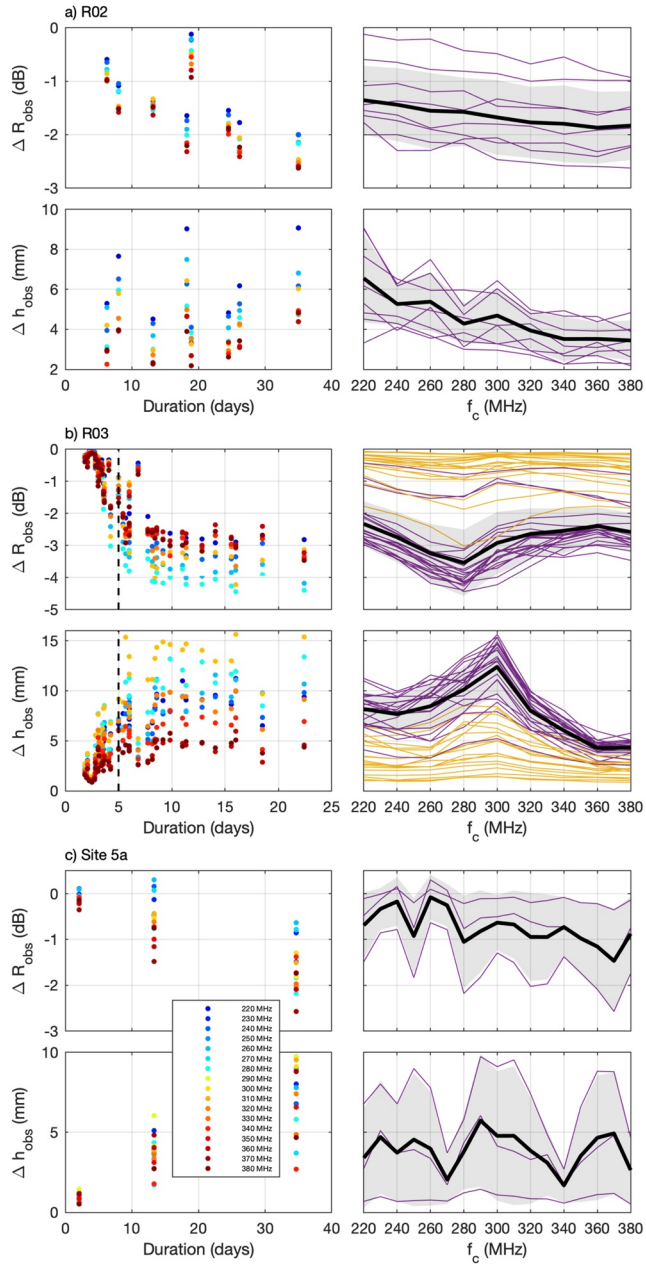

Figure 6. Dependence of accretion characteristics on center frequency (f_c). The left column shows the maximum amplitude drop (ΔR_{obs}) and the corresponding apparent accretion thickness (Δh_{obs}) for each accreted-ice event plotted against the event duration. The dots are colored according to the f_c used in the chirp processing. The right column shows the f_c dependence of ΔR_{obs} and Δh_{obs}; events longer/shorter than 5 days are in purple/yellow. The thick black line is the mean of the long events and the gray shading marks one std. dev.

For Site 5a, there were only three events detected over the single observed year; two shorter events, of 2 and 13 days, preceded a relatively long accreted-ice event lasting 35 days (Figure 6c). Despite the small number of events, a consistent pattern of ΔR_{obs} and Δh_{obs} emerges as f_c is varied. Its main feature is a non-monotonic f_c dependence, as for both quantities there are several local maxima and local minima.

3.4. Summary of Observations

The key observations from the ApRES time series are as follows:

1. At all three sites, the instances when the basal return amplitude is reduced coincide with instances when ice appears to be accreted at the ice-shelf base. The change in both quantities is relatively fast but smooth, that is, we do not observe a step change even when inspecting the unfiltered signal sampled at a 2-hourly rate
2. When ice appears to be accreted at the ice-shelf base, the rate of phase evolution may not be directly interpretable as a melt rate. The reason for that is the discrepancy between phase-based and amplitude-based melt rate derivations during accreted-ice events
3. The return amplitude reduction and apparent accretion depend on f_c. For R02, both quantities vary monotonically with f_c, but for R03 and Site 5a they do not

The occurrence and duration of accreted-ice events can be reliably identified from the ApRES data as episodes of decreased basal echo strength, coinciding with frequency-dependent melt rate estimates. However, further analysis is required to estimate the actual thickness and the electromagnetic properties of the accreted ice. Removing non-thickness-related phase changes from the apparent accretion and constraining the actual accretion thickness and properties is the subject of the following sections.

4. Three-Layer Model

4.1. Model Description

The f_c-dependent nature of the basal reflection during times of basal accretion can result from a change in electromagnetic properties at the ice-shelf basal boundary (via η), from the change in basal roughness (via S), or from both (see Equation 2). To constrain the a priori unknown relative permittivity and electrical conductivity of the accreted material, we consider a simple three-layer system consisting of glacial ice (g), accreted ice formed by the freezing of sea water (s), and ISW (w). Conceptually, the ice-shelf base changes between two states - the accretion-free melting periods and the accreted-ice events. During an accreted-ice event, there is always some accreted ice present, independently of whether there is active accretion or active melting taking place. During accretion-free melting the middle layer s is absent and during accreted-ice events, it is present (see schematic in Figure 7). The composition of the accreted ice in the layer s is unknown and it can be anything from consolidated marine ice to a slush formed by a mixture of frazil ice and ISW (e.g., as detected in a borehole drilled ~70 km southeast of Site 2 by Nicholls et al. [1991]). For simplicity we will refer to this layer as marine ice, regardless of its degree of consolidation, to emphasize that it contains ice formed by the freezing of sea water beneath an ice shelf while reserving the term sea ice for ice formed at an ice-shelf-free ocean surface. The basic constraint on the range of electromagnetic properties in s is that they should lie between those of g and w, for which the typical values of permittivity are $\epsilon'_g = 3.18$ and $\epsilon'_w = 81$, and typical

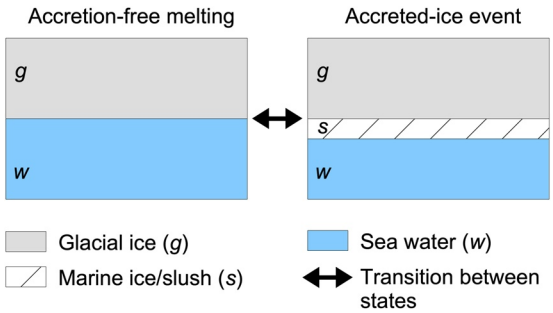

Figure 7. A schematic depicting the constituents during the two states of the ice-shelf base: accretion-free melting and accreted-ice events.

conductivity of glacial is $\sigma_g = 10^{-5}$ S/m (e.g., Morey & Kovacs, 1982). Sea water conductivity is available from past oceanographic profiles at Site 2 and it is $\sigma_w = 2.7$ S/m (A. Robinson et al., 1994).

As the ApRES signal propagates from the ice-shelf surface toward the base, it is partly reflected at the *gs* interface and partly transmitted. A second reflection occurs at the *sw* interface and again some part of that signal reflected from *sw* is transmitted at the *gs* interface. If the thickness of the layer *s* is less than the range resolution (Δr in Equation 1), the reflected and transmitted signals from the *gs* interface will be combined in the ApRES processing. The combined reflection coefficient of the three-layer system takes into account phase shifts from reflections at the *gs* and *sw* interfaces, attenuation from the two-way travel through the layer *s*, and a phase shift from the transmission at the *gs* interface. It is given as (e.g., Orfanidis, 2002)

$$R_{gsw} = \frac{\rho_{gs} + \rho_{sw} e^{2ik_s L_s}}{1 + \rho_{gs}\rho_{sw} e^{2ik_s L_s}}. \tag{5}$$

Here, ρ_{gs} and ρ_{sw} are elementary reflection coefficients at the *gs* and *sw* interfaces given by Equation 2; the factor of two in the exponents accounts for the two-way travel through the marine-ice layer of thickness L_s, where the wavenumber k_s is defined as

$$k_s = \frac{2\pi f_c \sqrt{\epsilon_s}}{c}. \tag{6}$$

We expect f_c-dependent differences in the sum of the two reflections in R_{gsw}, because the wavelength in the accreted layer *s* varies with f_c, and for a fixed L_s, this will result in different degrees of interference between the waves reflected from *gs* and *sw*. As the state of the ice-shelf base changes from accretion-free melting to an accreted-ice event, the base goes from a two-to a three-layered state, and the difference in the return amplitude in dB is

$$\Delta R = 20\left(\log_{10} |R_{gsw}| - \log_{10} |R_{gw}|\right) = 20 \log_{10} \frac{|R_{gsw}|}{|\rho_{gw}|}, \tag{7}$$

where $R_{gw} = \rho_{gw}$, because $L_s = 0$ m in the accretion-free state. $\Delta\theta$, the difference in the phase of the reflected wave associated with the change between the two states, is

$$\Delta\theta = \angle R_{gsw} - \angle R_{gw}. \tag{8}$$

To compare with thickness changes detected with ApRES (e.g., Figure 6), we convert $\Delta\theta$ to the change in thickness via (Brennan et al., 2014),

$$\Delta h = \Delta\theta \frac{c}{4\pi f_c \sqrt{\epsilon'_g}}, \tag{9}$$

where $\epsilon'_g = 3.18$, because that is the value originally used to construct the ApRES displacement and melt rate time series. The calculated Δh is an apparent thickness change because it includes the effects of both the actual thickness change between the two states (L_s) and the reflection phase shift that results from the insertion of a layer composed of a third, marine-ice material whose electromagnetic properties are different to those of *g* and *w*. The quantities ΔR and Δh constitute the output from the three-layer model and ApRES can measure them both.

Finally, the amount of pure accreted ice mass can be obtained by converting the accumulated marine-ice thickness L_s to a glacial-ice layer of equivalent mass with thickness L_g using a mixing model. A mixing model relates the effective dielectric constant of a mixture to the volume fraction of each of the components, assuming their individual dielectric constants are known. Here, the accreted ice can be thought of as a

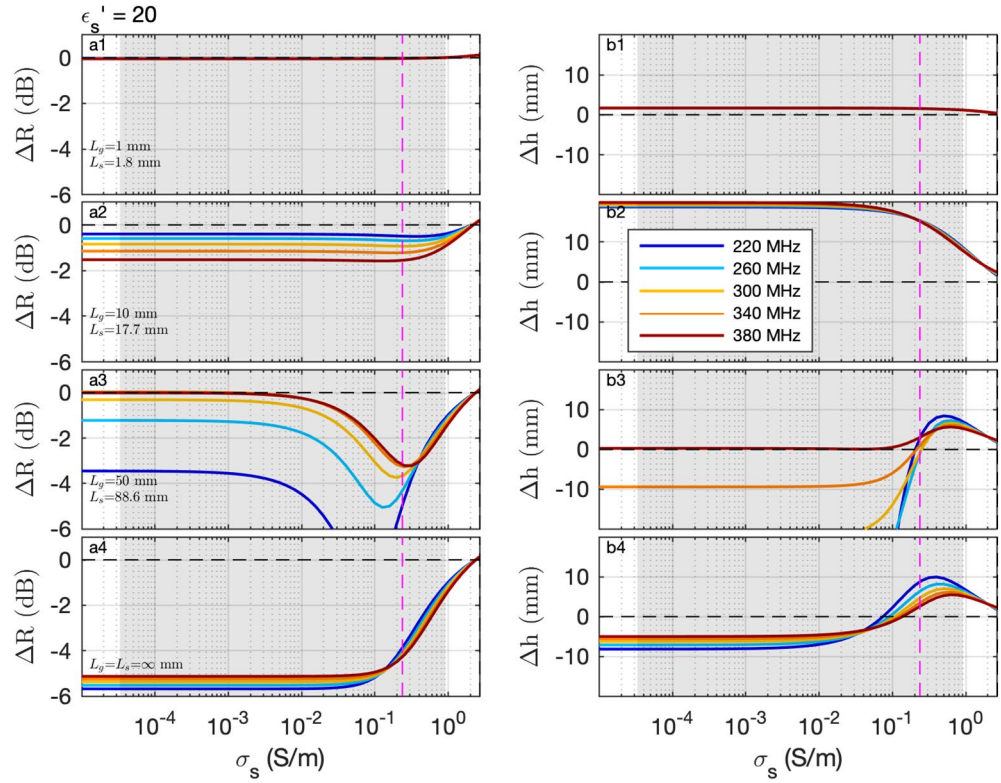

Figure 8. Examples of changes in basal return amplitude (ΔR) and apparent accretion (Δh) as a marine-ice layer of thickness L_s, dielectric constant $\epsilon_s' = 20$, and a range of conductivities σ_s, is inserted between ice and ocean; L_g is equivalent glacial ice thickness. The σ_s that lie within the Hashin and Shtrikman (1962) bounds are shaded in gray, and the σ_s that would result from the Looyenga (1965) mixing model is marked with dashed magenta line. Horizontal black dashed line shows where ΔR and Δh are zero, and the σ_s limits are the conductivities of glacial ice and sea water. If the electromagnetic properties of the marine-ice layer are close to those of glacial ice or if the layer is thin, the non-thickness related phase change is small and $\Delta h \sim L_s$.

mixture of salty liquid ISW and fresh solid glacial ice. Knowing the dielectric constants of the components g and w and of the mixture s yields volume fraction of the glacial ice v_g in s, and gives the equivalent glacier thickness $L_g = L_s v_g$. The quantity L_g is more useful than L_s, because the pure accreted ice mass can be constrained physically using knowledge of the geographic and oceanographic settings of each site. There are several mixing models available; theoretical bounds on the volume fraction of the constituents are provided in Hashin and Shtrikman (1962). Here, we use the formula derived by Looyenga (1965), which lies within these bounds. This model is suitable for homogeneous mixtures and it is commonly used in glaciology applications. The formulation is symmetric with respect to the order of components in the mixture and it lies close to the average of the broad sweep of the available mixing models. Looyenga (1965) calculates the glacial volume fraction v_g as

$$v_g = \frac{\epsilon_s'^{\frac{1}{3}} - \epsilon_w'^{\frac{1}{3}}}{\epsilon_g'^{\frac{1}{3}} - \epsilon_w'^{\frac{1}{3}}}. \tag{10}$$

4.2. Model Properties

Before using the three-layer model to constrain the changing basal properties at the three RIS sites, we explain the expected behavior of the model outputs, ΔR and Δh, as ϵ_s', σ_s, L_g, and f_c vary. In Figure 8, we show examples for a fixed value of $\epsilon_s' = 20$ (~55% ice) that focus on variations in the remaining three parameters. The figure explores how ΔR and Δh depend on σ_s for five values of f_c varied between 220 and 380 MHz to

Table 1
Observational Constraints on the Maximum Amplitude Drop (ΔR_{obs}) and Apparent Accretion Thickness (Δh_{obs}) for a Typical Accreted-Ice Event at Each Site Formulated Based on Figure 6

Label	Constraints	R02	R03	Site 5a
	ΔR_{obs} *constraints*			
R1	sign of ΔR_{obs} for all f_c	Negative	Negative	Negative
R2	ΔR_{obs} dependence on f_c	ΔR_{obs} decreases with f_c	Local min at 280 MHz	Local min at 250 and 370 MHz local max at 230 and 260 MHz
R3	$\max_{f_c} \Delta R_{obs} - \min_{f_c} \Delta R_{obs}$	$\geq$ 0.5 dB	$\geq$ 1 dB	$\geq$ 1 dB
R4	$\min_{f_c} \Delta R_{obs}$	≥ -3 dB and ≤ -1.5 dB	≥ -6 dB and ≤ -3 dB	≥ -3 dB and ≤ -1 dB
	Δh_{obs} *constraints*			
h1	sign of Δh_{obs} for all f_c	Positive	Positive	Positive
h2	Δh_{obs} dependence on f_c	Δh_{obs} decreases with f_c	Local max at 300 MHz	Local min at 270 and 340 MHz Local max at 230 and 290 MHz
h3	$\max_{f_c} \Delta h_{obs} - \min_{f_c} \Delta h_{obs}$	$\geq$ 2 mm	$\geq$ 5 mm	$\geq$ 4 mm
h4	$\max_{f_c} \Delta h_{obs}$	$\geq$ 3 mm and $\leq$ 15 mm	$\geq$ 7 mm and $\leq$ 20 mm	$\geq$ 3 mm and $\leq$ 15 mm

remain consistent with the ApRES settings. This is repeated for a number of L_g values, varying between 1 mm and ∞. The case of $L_g \to \infty$ is effectively where the accreted material is sufficiently thick and lossy that the reflected wave from the *sw* interface is absorbed before reaching the *gs* interface. The main effect of changes in ϵ_s' would be to introduce an offset and to stretch along the vertical axis the curves of ΔR and Δh plotted as a function of σ_s in Figure 8, because with increasing ϵ_s' the actual thickness of the accreted layer L_s increases for a fixed L_g. Thus the general features we describe for the case of $\epsilon_s' = 20$ also hold for the relevant range of ϵ_s' between 3.18 and 81 (see Figures S2 and S3).

When the accreted-ice layer is very thin, the variations in ΔR and Δh with σ_s and f_c are minimal (Figures 8a and 8b). Especially if the electromagnetic properties in *s* are close to those of *g*, the small contrast in the properties leads to only small non-thickness related phase change, and $\Delta h \sim L_s$. The non-thickness related phase change becomes important only for large σ_s, resulting in Δh significantly less than L_s. As the accreted layer thickness increases, the effects of σ_s and f_c become important (Figures 8a and 8b). The different wavelengths associated with varying f_c contribute to different phase shifts and attenuations as the wave travels through a thicker accreted layer, and the difference between Δh and L_s becomes significant for increasingly lower σ_s as L_s increases. In the limiting case of an infinite thickness of the marine-ice layer, Δh becomes independent of L_s and completely determined by the non-thickness related phase changes (Figure 8b). For both small and very large L_g, the variation with f_c is monotonic for most σ_s. The exception to this are short intervals of σ_s values surrounding the reversal of the f_c dependence from monotonic increase to monotonic decrease, or the reverse. There are one or two such locations for both ΔR and Δh, but they do not necessarily occur over the same σ_s for the two variables.

The transition between small and very large L_g is characterized by accretions that are thick enough to allow significant constructive and destructive interference within the layer *s*. Because the interference pattern depends on the wavelength in the medium, the results depend strongly on f_c (via Equation 6). The f_c-dependence of ΔR and Δh can be non-monotonic (Figures 8a and S3) and it is sensitive to L_g. The convergence to the limiting case of $L_g \to \infty$ is controlled by σ_s, which determines the attenuation of the signal via the complex part of the relative permittivity (Equation 4). Attenuation is fastest for highest σ_s, because the rate at which the signal strength is attenuated within *s* increases exponentially with σ_s via Equation 5. Conversely, for small σ_s the dielectric loss in *s* is low and a much larger L_g is needed to absorb sufficiently the reflection from the *sw* interface (Figure 8a).

5. Constrained Basal Accretion

We now apply the three-layer model to simultaneously constrain ϵ_s', σ_s, and L_g at the ApRES sites. Our objective is to identify typical accretion properties at each site, rather than to analyze each accreted-ice event individually, therefore we focus on the characteristic f_c-dependence across all the events at each site. Further, we aim to identify properties of the final accreted-ice layer at the end of an active accretion period and not over the full course of the transition between the two states. The observables with which we constrain the calculated ΔR and Δh are ΔR_{obs} and Δh_{obs} from Figure 6. ΔR_{obs} and Δh_{obs} represent the change from the accretion-free state to the state when the accreted layer fully developed, which occurs when the return-amplitude drop and apparent accretion reach their highest magnitudes. Using ΔR_{obs} and Δh_{obs} from all detected events we formulate a set of constraints for a typical accretion event at each site and list them in Table 1. The constraints reference the sign of ΔR_{obs} (R1), the f_c-dependence of ΔR_{obs} (R2), the difference between the maximum and the minimum ΔR_{obs} (R3), and the minimum observed ΔR_{obs} (R4). The constraints for Δh_{obs} are analogous to those for ΔR_{obs} (h1-h4 in Table 1). To identify the accretion properties at each site, we consider a range of all possible ϵ_s', σ_s and L_g, and for each combination of these parameters we evaluate whether the output of the three-layer model (Equations 7 and 9) satisfies the observational constraints for the given site.

5.1. R02

The accretion results for R02 are shown in Figure 9. For each example L_g the model output is shown as a differently colored contour enclosing a plausible combination of σ_s and ϵ_s' that satisfies the observational constraints in Table 1. There are many possible solutions, and to identify which are physically reasonable we impose constraints from a mixing model. The contours which intersect the dashed magenta line in Figure 9 are consistent with the Looyenga (1965) formulation, which is appropriate for homogenous mixtures, and which we assume provides an accurate model of the properties of the ice-ocean mixture. However, as we cannot be sure about the level of heterogeneity, given the lack of information about the structure of the accretion, we also plot the Hashin and Shtrikman (1962) bounds.

First, we assume that reflections from both interfaces are specular (i.e., $S_{gw} = S_{gs} = S_{sw} = 1$ in Equation 2) and plot the results in Figure 9a and further details in Figure S5. The range of possible combinations of σ_s and ϵ_s' that are consistent with observations can be separated into two groups. The first group (the dark blue contours in Figure 9a) consists of L_g limited to only a few mm. These low L_g require the dielectric constant

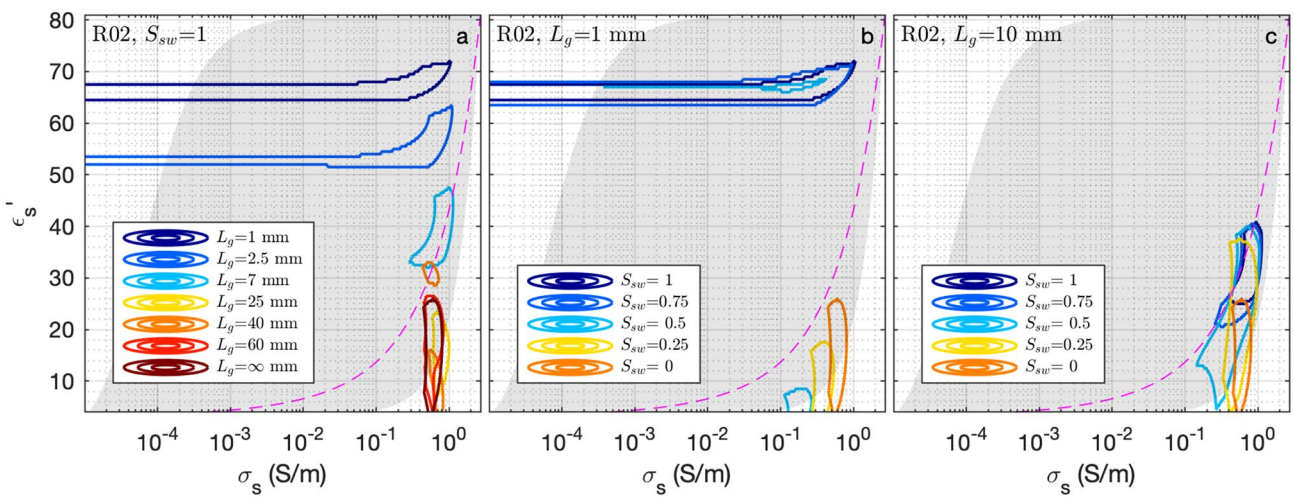

Figure 9. Electromagnetic properties of accreted marine ice consistent with ApRES observations at R02. Contours enclose regions where the three-layer model output satisfies the constraints from Table 1 for given L_g and S_{sw}. (a) The equivalent glacial ice thickness L_g of the accreted marine-ice layer is varied, while assuming the reflection from both material interfaces is specular. (b) L_g is kept at 1 mm (this translates to different marine-ice thickness L_s for different ϵ_s') and the roughness at the marine-ice/ice-shelf water interface, S_{sw}, is varied. (c) Same as b but for L_g = 10 mm. As in Figure 8 the region of plausible σ_s are shaded in gray, and the dashed magenta line marks σ_s consistent with the mixing model of Looyenga (1965). The most likely solutions lie on the intersection between the colored contours and the dashed pink line.

to be high ($\epsilon_s' \gtrsim 50$), making L_s tens of mm thick, and at the same time they allow for a broad range of σ_s, covering five orders of magnitude all the way from $\sigma_s = \sigma_g$ up to $\sigma_s \sim 1$. However, for an agreement with the Looyenga (1965) mixing model, at these small L_g and high ϵ_s' values the σ_s would need to be closer to 2 S/m, which is approximately twice as high as the highest σ_s value consistent with the observations. Therefore, the small L_g values of less than 5 mm do not provide a satisfactory solution. The second group of possible combinations (light blue, yellow and orange contours in Figure 9a) consist of a broad range of accretion thicknesses ($L_g \gtrsim 5$ mm) and dielectric constants ($10 \lesssim \epsilon_s' \lesssim 50$) but the range of required conductivities is tight: 0.1 S/m $\lesssim \sigma_s \lesssim$ 1 S/m. These relatively high σ_s values are largely independent of the remaining parameters. Parts of this region of high σ_s that are consistent with the observations also lie within the constraints of the Looyenga (1965) mixing formula. Therefore, the desired solution lies within this second group of possible combinations of properties. There are two subsets of solutions: one in the range of L_g of 5–12 mm, ϵ_s' of 32–46 and σ_s of 0.6–1 S/m; and the other one in the range of L_g of 37–50 mm, ϵ_s' of 28–34 and σ_s of 0.4–0.6 S/m.

To investigate the sensitivity of the results to the roughness of the marine-ice/ISW interface, we consider a case when S_{sw} is allowed to vary. To visualize this, we fix L_g and look for possible combinations of ϵ_s', σ_s and S_{sw}, consistent with the observational constraints. As in Figure S4, S_{sw} is kept real and it is varied from 1 to 0. Figures 9b and 9c show the results for L_g of 1 and 10 mm, respectively. We find that the results are qualitatively similar to the specular case, with the two groups of possible parameter combinations still present. As S_{sw} decreases for the thin case ($L_g = 1$ mm), the set of plausible combinations of electromagnetic properties moves from the first group (high ϵ_s' and broad range of σ_s) to the second group (lower ϵ_s' and high σ_s). The transition between the two states associated with the S_{sw} decrease avoids the mixing line given by Looyenga (1965) (magenta line in Figures 9b and S6), which means that low values of L_g still are not an acceptable solution. For the thicker case ($L_g = 10$ mm), higher S_{sw} values are consistent with higher ϵ_s' and lower S_{sw} with lower ϵ_s', but overall the variations in S_{sw} have a relatively limited effect (Figure 9c).

The results in Figure 9 imply that the accreted-ice layer at R02 has a relatively high σ_s. This implies that as the ice-shelf base transitions from accretion-free melting to a developed accreted-ice layer, the contribution of non-thickness related phase change to the apparent thickness will be significant even for relatively small L_g. In practice this means that Δh will differ significantly from L_s (e.g., see Δh over the 0.1 S/m $\lesssim \sigma_s \lesssim$ 1 S/m range in Figure 8b2). This confirms that the phase shifts associated with the appearance of the accreted ice need to be considered for accurate estimation of the marine-ice layer thickness.

5.2. R03 and Site 5a

When repeating the same analysis for R03 and Site 5a, we find that for neither site the three-layer model yields a solution that would be consistent with the respective observational constraints ΔR_{obs} and Δh_{obs}, even before imposing any mixing model assumption. The lack of solutions holds for both the specular case and the case when S_{sw} is real and independent of f_c. This result arises because the variation of ΔR_{obs} and Δh_{obs} with f_c is non-monotonic for both R03 and Site 5a (see Figures 6b and 6c, right column). Figure 10 illustrates the problem for the case of R03. We impose two different subsets of the observational constraints from Table 1 and look for model solutions consistent with each of the subsets separately. The first subset includes all constraints except for the f_c dependence of ΔR and Δh (constraints R2 and h2 are excluded). In this case, the results for R03 would be similar to those of R02 (Figure 10a). The second subset includes only the ΔR and Δh sign (constraints R1 and h1) and the f_c dependence of ΔR and Δh (constraints R1 and h2). With this second reduced set of constraints, there are no longer any suitable σ_s, ϵ_s', and L_g combinations (Figure 10b), confirming that the f_c dependence of the observables is the constraint causing the difficulty.

There are two ways in which the model can yield a non-monotonic f_c dependence of either ΔR or Δh. One way comes from the relatively narrow intervals of σ_s over which the f_c dependence for a given ϵ_s' and L_g changes from increasing to decreasing or vice versa (e.g., see Figure 8). However, these σ_s intervals are generally different for ΔR and for Δh. Therefore, even if there exists a narrow region of σ_s and ϵ_s' that is consistent with the observed non-monotonic f_c dependence for ΔR (Figure 10b for R03), the respective σ_s and ϵ_s' region for Δh is different (Figure 10b), giving no overlap (Figure 10b). Another way to obtain a non-monotonic f_c dependence for ΔR or Δh is when L_s is sufficiently large to allow complete cancellation between the

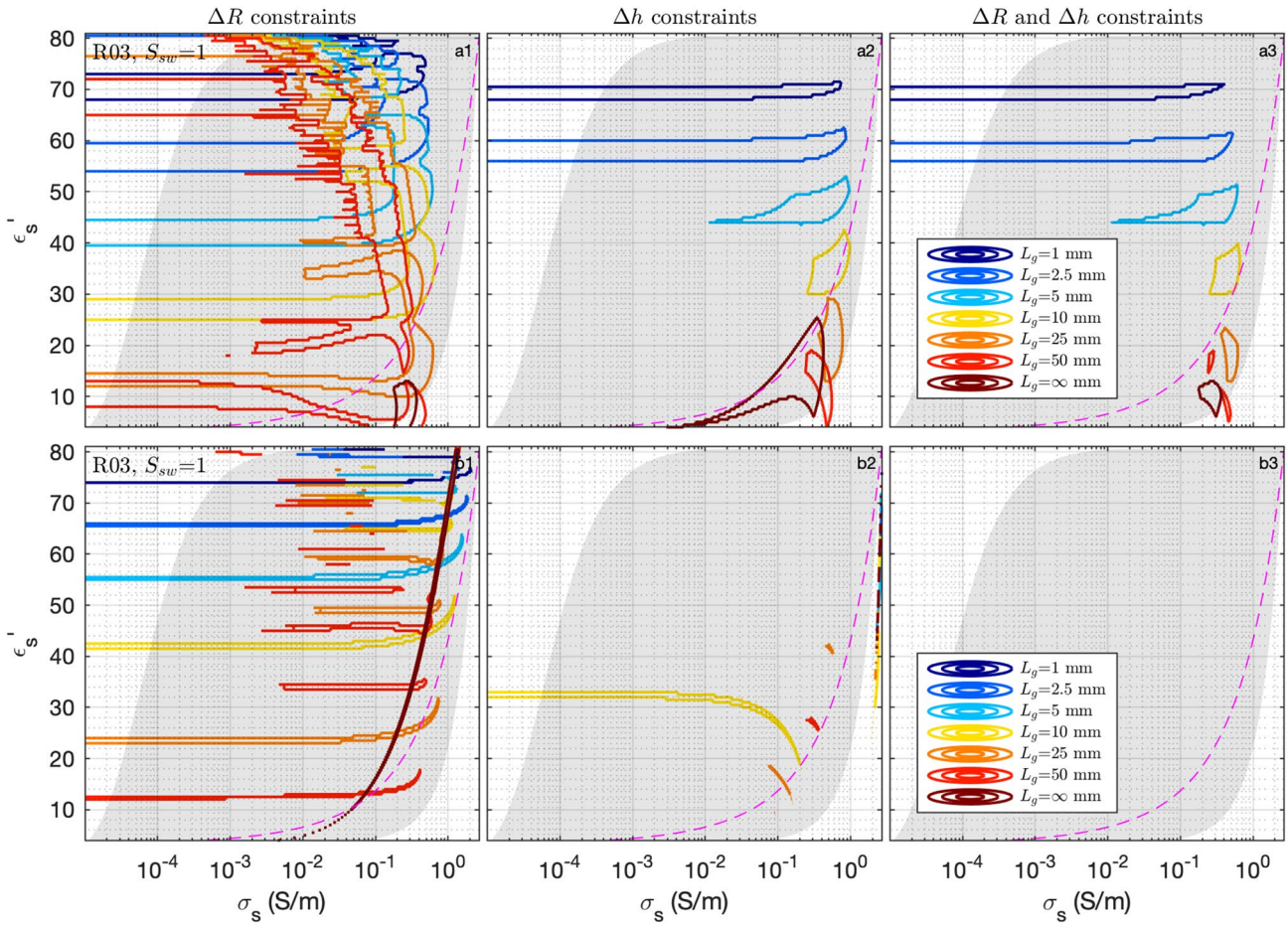

Figure 10. Electromagnetic properties of accreted marine ice consistent with different constraints derived from ApRES observations at R03. As in Figure 9 contours enclose regions that satisfy a set of the constraints from Table 1. To show the effect of different constraints separately, on the left panels only ΔR constraints are imposed, in the middle only Δh constraints, and on the right both ΔR and Δh constraints are imposed simultaneously as in Figure 9. (a) All constraints from Table 1 were imposed except for R2 and h2. (b) Only the constraints R1, R2, h1, and h2 from Table 1 were imposed.

waves reflected from both interfaces. The resulting interference of the waves depends on the wavelength, and a non-monotonic f_c dependence can appear (e.g., Figures S3a and S3b). However, as in the first case it is difficult to satisfy the observed f_c dependence for both ΔR and Δh simultaneously.

A simple way to reconcile the observations from R03 and Site 5a within the simple three-layer model framework, is to consider an interface that is rough on scales giving an f_c-dependence in the reflection coefficient via the roughness parameter S introduced in Equation 2. So far we have only shown examples where S_{sw} is real and constant, but in general S_{sw} is a complex quantity and can vary with f_c in a way that modulates both the amplitude and the phase of the basal reflection. Agreement with the observations from R03 and Site 5a would require the roughness parameter to be a function of f_c at least at one of the two interfaces (S_{gs} or S_{sw}). It is clear that by making an appropriate choice of non-monotonic S at either interface, we can obtain a non-monotonic ΔR and Δh that satisfies the observations. However, allowing S to change with f_c results in the problem being poorly constrained and it is no longer possible to provide tight bounds for σ_s, ϵ_s' and L_g.

A closer look at the basal returns in the ApRES signals reveals evidence of site dependent basal roughness. Figure 11 shows the way the shape of the basal echo and the location of the first basal reflection vary with f_c. The R02 basal reflection consists of a single, well defined peak whose shape and location varies little with f_c (Figures 11a and 11b). R03 also has a strong first basal reflection, but both its width and location vary with f_c more than in the R02 case (Figures 11a and 11b). The basal echo from Site 5a has a considerably more complicated signal than from the previous two sites (Figure 11a). It features a long trailing edge as a sequence of

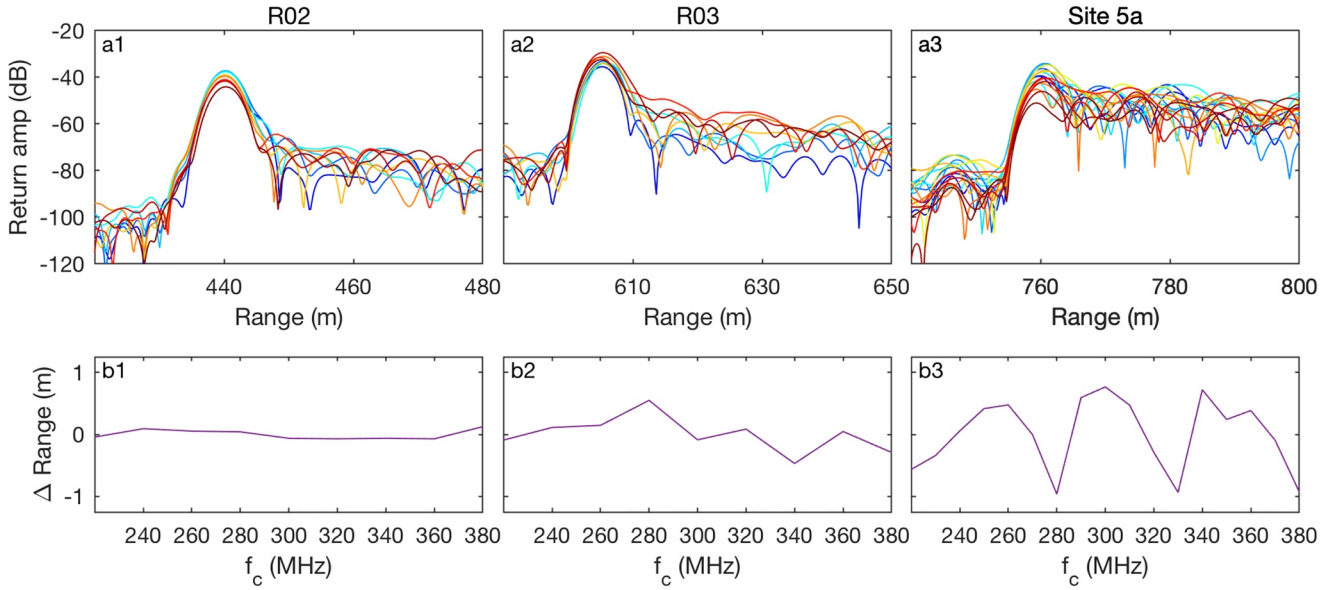

Figure 11. Basal roughness indicators. (a) A shot of return amplitude profile near the ice base for different center frequencies (f_c) using 40 MHz bandwidth as in Figure 6. (b) Variation in range of the first basal peak as a function of f_c.

elevated returns past the first basal reflection. Also the location of the first reflection is strongly dependent on f_c (Figure 11b3). Together these indicate elevated basal roughness (Robin et al., 1969). Figure 11 shows that elevated basal roughness is present at both R03 and Site 5a, and that its manifestation changes with f_c, thus providing qualitative support for the hypothesis that the complex roughness parameter S varies with f_c at these two sites. The accretion properties at these sites cannot be quantified until an additional observable, that would accommodate the additional degree of freedom introduced by the f_c dependence of S, becomes available.

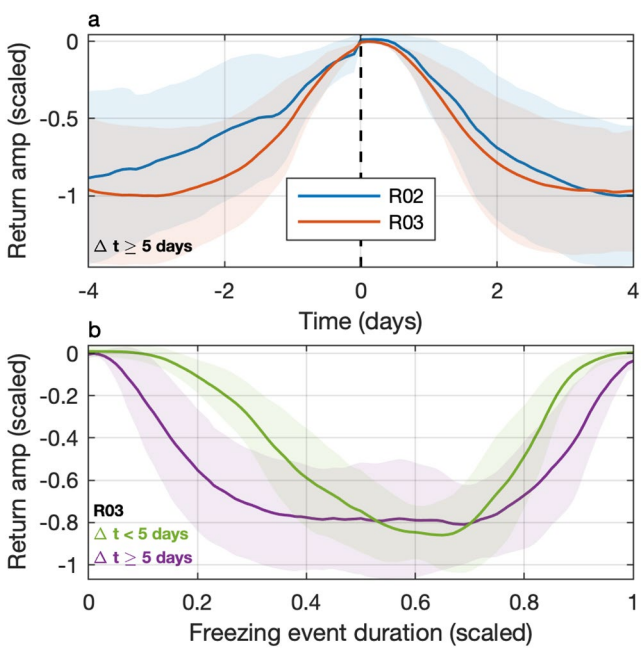

Figure 12. Accreted-ice event composites at R02 and R03: (a) Return-amplitude drop composites of the last four and the first four days of accreted-ice events, the return amplitude is normalized to allow site-to-site comparison (only events longer than 5 days are included). (b) Normalized return-amplitude drop composites at R03. The accreted-ice events were grouped into long and short events with a $\Delta t = 5$ day cutoff, as a motivated by Figure 6. Shading shows one std. dev. in all panels.

6. Discussion

6.1. Basal Accretion Mechanisms

To identify the mechanism causing the observed intermittent basal accretion, we estimate bounds on accretion rates for different processes and compare them with accretion rate estimates for R02. The observationally constrained three-layer model produced a range of plausible values of L_g, the equivalent glacial ice thickness of a developed accreted-ice layer. L_g can be converted into a mean accretion rate using an estimate of a typical time over which the accretion builds up. A typical event begins and ends relatively abruptly, as shown by a composite of return amplitudes for accreted-ice events in Figure 12. The reader is reminded here that the return amplitude time series have not been low-pass filtered. For longer events, the return amplitude generally levels off once a minimum has been attained, although occasionally there are fluctuations. At R02 it typically takes less than 4 days to reach the minimum amplitude. Using the lower subset of L_g estimate of ~5–12 mm gives mean accretion rate of ~1–3 mm/day, but for the higher plausible values of L_g of ~37–50 this can be as high as ~9–13 mm/day.

Accretion at the ice base requires a heat sink. That can be provided either by the ice shelf or by the ocean. When heat loss occurs primarily through the ice shelf, congelation ice is formed, growing from the base toward the

ocean. Alternatively, when supercooled water is brought to the ice-shelf base, freezing is sourced from the ocean, and frazil ice may form in the water column and precipitate onto the ice base in addition to growing from the base directly. Next, we estimate bounds on accretion rates from these two mechanisms and evaluate them against the derived accretion rates for R02.

6.1.1. Congelation Ice

When freezing is governed by heat loss through the ice shelf, the accretion rate is proportional to the ice-shelf vertical temperature gradient at the ice-ocean boundary. The vertical profile of ice-shelf temperature can be found from an advection-diffusion model, whose steady state solution takes an explicit form that depends on the mean melt rate, surface and basal temperatures, and a number of well-known constants (Holland & Jenkins, 1999). To estimate congelation ice rates of accretion in R02-like conditions, we use past observations from Site 2, located between sites R02 and R03 (Figure 1a). Approximate Site 2 values of ice-shelf surface temperature and boundary layer salinity are −25°C and 34.6 psu, respectively (A. Robinson et al., 1994; Nicholls, 1996). Ice-shelf basal temperature is assumed to be at the freezing point, determined by the depth of the ice-shelf base and the salinity measurement nearest to the Site 2 base. Data from thermistors frozen into the ice shelf at Site 2 fit well the advection-diffusion model for a melt rate of ~0.28 m/a (Figure S7a). The mean melt rates for R02 and R03 are similar, near 0.4 m/a, resulting in a temperature gradient at the ice-shelf base of ~−0.25°C/m and steady-state accretion rate of ~0.14 mm/day (or ~0.6 mm accretion in 4 days, Figure S7c), approximately 10 times lower than the lower bound for accretion rates inferred from the R02 ApRES observations. Melt rate variations can cause short term variations in temperature gradient near the ice base, which can be significant over shorter periods (Stewart, 2018), but these cannot last over multi-day accretion events and account for the much higher ApRES-inferred accretion rates. The relatively slow congelation ice growth estimate of a couple of cm per year at the RIS sites is consistent with accretion rate observations and estimates at the J-9 site at the Ross Ice Shelf, where accretion is known to be governed by heat loss through the ice shelf (Zotikov et al., 1980).

The J-9 site observations also provide the primary source of information about the properties of congelation ice beneath ice shelves. There, the salinity measurements of the accreted ice yielded 2–4 psu and the ice was well consolidated, implying that it's dielectric constant ϵ_s' should be near that of glacial ice. Zotikov et al. (1980) does not report the conductivity of the accreted ice. The closest available conductivity measurements are those of sea ice formed at the ocean surface, where typical salinities are 3–10 psu, conductivities 0.01–0.1 S/m, and dielectric constants 3.5-6 (Morey et al., 1984; Weeks & Ackley, 1982). As Figure 9 shows, the combination of electromagnetic properties and accreted ice thickness required for congelation ice accretion (low ϵ_s' and $L_g < 1$ mm) does not lie in the space of combinations consistent with the R02 observations. Assuming the J-9 congelation ice characteristics are also representative of the RIS environment, we conclude that congelation ice is not the main type of accreted ice that we have detected in our measurements. However, even if congelation ice cannot grow sufficiently fast to fully explain the measurements at R02, it is still expected to form in parallel with frazil ice whenever ISW at or below the local freezing point is present at the ice-shelf base.

6.1.2. Frazil Ice

R02, R03, and the historic site Site 2 are located along the eastern flank of the Ronne Depression. They lie between two regions of significant marine-ice mass resulting from persistent accretion upstream, caused by ISW outflows rising along the steep ice-shelf base near the grounding lines (Figure 1a). However, outflowing ISW can be detected all the way to the ice-shelf front at two main locations, one at the eastern margin of the Ronne Depression, and the other at the western most point along the ice front (Gammelsrød et al., 1994; Nicholls et al., 2003). Although the ice base at both R02 and R03 is melting on average, intermittent accretion could occur at these sites through lateral displacement of outflowing ISW along the base of the eastward thinning ice shelf. We estimate the rate of frazil ice growth from lateral ISW displacements as follows. The mass of ice per unit width M_g formed from the mass of water per unit width M_w supercooled by ΔT is given by

$$M_g = M_w \frac{c_{pw}\Delta T}{L_f}, \tag{11}$$

where c_{pw} is the specific heat capacity of water and L_f is the latent heat of fusion. Assuming that M_g is evenly distributed over a distance d_x, the rate at which the ice thickness can grow is given by

$$\frac{\partial h}{\partial t} = \frac{\partial M_g}{\partial t}\frac{1}{d_x \rho_g} = \frac{u d_z \rho_w}{d_x \rho_g}\frac{c_{pw}\Delta T}{L_f}, \tag{12}$$

where we have used the relation $\frac{\partial M_g}{\partial t} = u d_z \rho_w$. Here, ρ_g and ρ_w are ice and water densities, u is water flow velocity along d_x, and d_z is the thickness of the supercooled layer. ΔT and d_x can be estimated from the eastward thinning slope of the ice base which is comparable at the three sites and is, on average it changes by ~1 m for every 1 km. For d_x of 20 km this gives 0.015°C of supercooling. Nicholls (1996) indirectly estimated the background flow at Site 2 to reach about 0.06 m/s, which we use as an estimate of u. The most uncertain variable is the thickness of the supercooled water mass d_z. Using a value of $d_z \sim 20$ m gives ice thickness growth of over 1 mm/day, which implies that frazil ice can easily grow eight or more times faster than congelation ice. Comparison with the historic Site 2 oceanographic measurements (Figure S8) shows that our estimates for ΔT and d_z are realistic and rather conservative, suggesting that the frazil ice growth there could be even faster than our rough estimate of ~1 mm/day. The ApRES-derived accretion estimates with accretion rates of 1–3 mm/day for R02 are, therefore, consistent with physical constraints for lateral ISW water displacements along the ice-shelf base. The accretion estimates of 9–13 mm/day were also consistent with the model and observations, however, they are too high given the physical and geographical constraints. Therefore, we do not consider these high accretion estimates plausible and reject them.

Having shown that the frazil ice formation rates are consistent with inferred accretion rates at R02, we now investigate whether the inferred electromagnetic properties are also consistent with those of frazil ice. The process by which frazil ice crystals deposit onto the ice-shelf base is gradual and initially inefficient in salt removal. As frazil ice crystals precipitate, ISW remains trapped between them, forming a slush whose bulk electromagnetic properties will be much closer to those of ISW than in the case of congelation ice. Such a slush layer can be up to ~14 m thick (Nicholls et al., 1991). The inferred electromagnetic properties at R02 of ϵ_s' above 20 and σ_s above 0.1 S/m are well above typical sea-ice values, supporting the hypothesis that the accreted ice at the base is not well consolidated.

There is additional supporting evidence for frazil ice deposition being the dominant mechanism for intermittent basal accretion along the eastern flank of the Ronne Depression. Past oceanographic measurements at Site 2 (A. Robinson et al., 1994) included several salinity profiles that were contaminated in ways typical of environments with suspended frazil in supercooled water (N. J. Robinson et al., 2020). Because different profiles collected several days before and several days after these contaminated profiles showed a regime change near the ice-shelf base, it was concluded that the inferred presence of frazil ice was real and transitory. Finally, frazil ice deposition presents a plausible mechanism for explaining the differences between the build up time of short and long accreted-ice events observed at R03 (Figure 12b). While for events longer than ~5 days the duration over which ice thickness is built up and destroyed is approximately the same, for events shorter than ~5 days ice is grown relatively slowly compared with the rate at which it is removed. The rate at which crystals deposit is proportional to their concentration, which is caused by the amount of water and its degree of supercooling. We believe it is reasonable to expect weaker and shorter events to build up relatively slowly.

6.2. Oceanographic Context

The accreted-ice events at R02 are relatively few and they are associated primarily with a seasonal melt rate decrease. These dynamics will be analyzed in more detail in a follow up paper.

The accreted-ice events at R03 are relatively frequent and occur throughout the year. The frequency and duration of the events occur at a comparable timescale to the baroclinically forced temperature fluctuations observed at Site 2 by Nicholls (1996). It is therefore likely that R03 and Site 2 are both in the same regime, dominated by mesoscale variability.

There were only three accreted-ice events identified at Site 5a. As we were not able to estimate the accretion properties at this site, we do not have sufficient constraints to identify the accretion mechanism. Site 5a

is located in an oceanographic setting different from that of R02 and R03, and the mean melt rate there is twice as high as at the other sites. Although mesoscale variability has also been observed at this site, it did not involve routine displacement of ISW that would lead to supercooling (Nicholls, 2018). It is, therefore, possible that the accreted-ice events at this site were caused by the formation of congelation ice due to decreased flow speeds or temperatures in the ocean beneath.

6.3. Limitations

We have limited our quantitative analysis of the accretion properties to a three-layer setting. Therefore, our results characterize only the bulk electromagnetic properties of the accreted-ice layer formed by the freezing of ISW. In reality, accreted ice could be spatially heterogeneous, and there may be variations of electromagnetic properties with depth. However, our limited dataset does not justify a more sophisticated model, with the concomitant increase in the number of degrees of freedom.

We inferred the properties of a developed accreted-ice layer and the mean accretion rates, but we did not attempt to interpret the variability in the reflected phase during an accreted-ice event as melt rate variability. This is because variations in phase in the presence of accreted ice can be caused not only by thickness changes but also by an evolution of electromagnetic properties within the accreted layer. For example, consolidation and salt removal is an ongoing long-lasting process eventually leading to marine-ice formation. Although we only observe transitory accretion, we may be able to witness the beginnings of the consolidation process during which electromagnetic properties and accreted layer thickness change simultaneously. However, these simultaneous small variations in properties are difficult to separate out from the ApRES signal. Although we have not been able to derive detailed melt rate variability during accreted-ice events, the long-term melt rate estimate is unaffected by the lack of melt rate variability information during this time period, simply because the net basal-ice gain over an accreted-ice event must be zero.

Our technique for inferring simultaneously the accreted ice thickness and electromagnetic properties can yield many solutions. For R02, we have chosen one set of solutions over another by imposing a mixing model condition. We have assumed that the Looyenga (1965) mixing formula (Equation 10), is appropriate for the frazil ice depositing on the ice-shelf base at R02 over the course of a few days. However, if the heterogeneities in the accreted-ice layer were significant, a different mixing model may be more suitable with implications for the final accretion rate estimates. As we do not have direct observations of the crystal sizes and density at this site, the validity of the Looyenga (1965) formulation remains an assumption.

We do not have concurrent in-situ measurements to compare our findings of intermittent accretion rates with an independent estimate. A meaningful measurement to compare against would need to be collected in-situ, and therefore require a borehole. Ultimate confirmation of our findings may require optical imagery capable of providing quantitative estimates of accretion rates and evolution of the basal topography and roughness, combined ideally with laboratory analysis of the electromagnetic properties of an accreted-ice sample.

7. Implications for Other ApRES Applications

7.1. Improved Mean Vertical Strain Rate Estimates

The largest uncertainty in melt rates derived from a phase-sensitive radar usually comes from the poorly constrained motion of internal reflectors, whose displacements are used to identify the vertical strain rate profile needed to correctly calculate the non-melt contributions to total thickness change. If the internal reflections are strong throughout the ice column and well correlated from one shot to the next, this uncertainty is negligible. However, if reflections become weak at depth, which is often the case, there is a need to fit a vertical strain rate model to the strong reflectors higher in the ice column and extrapolate it to the ice base. This then yields an estimate of the non-melt contribution to total thickness change. The uncertainty can be formally quantified from the method used for the fitting of the model coefficients, for example, the least squares. The uncertainty in the functional form of the vertical strain rate is more difficult to assess. At times different assumptions of vertical strain rate profiles fitted to the limited number of internal reflections can lead to significantly different melt rate estimates (Jenkins et al., 2006; Vaňková et al., 2021). Near flexure

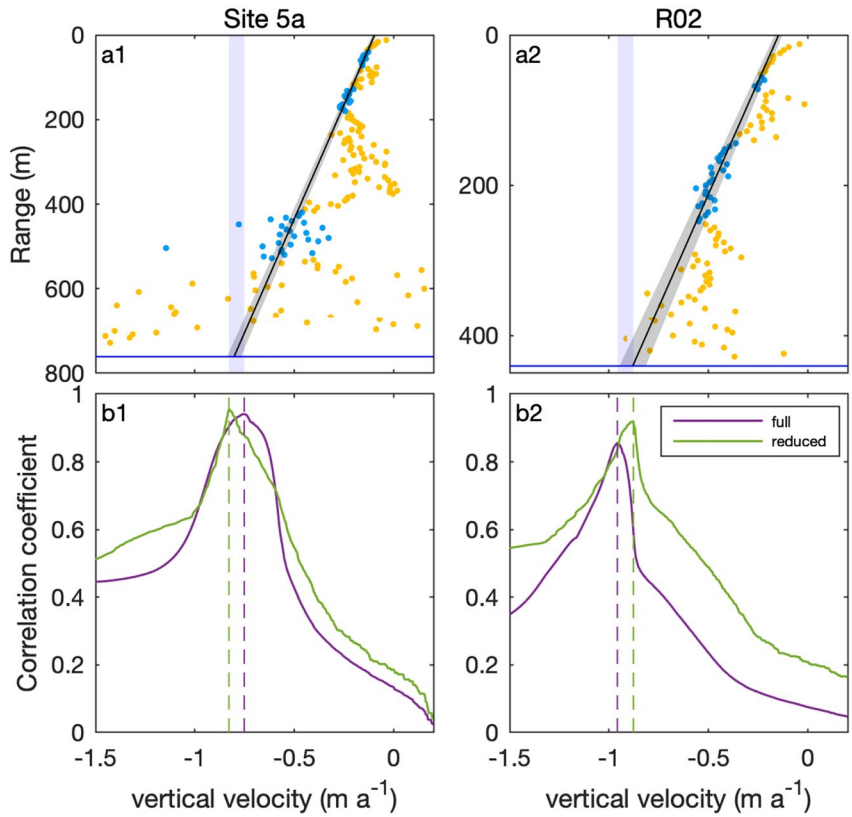

Figure 13. Estimation of non-melt basal displacement rates. (a) Mean line-of-sight displacement of internal reflectors (yellow dots), a subset of those (blue dots) was fitted with a constant vertical strain rate profile (black line with gray shading showing standard error). The intersection of the black line with the base (blue horizontal line) is the non-melt basal displacement rate. The vertical blue shading marks the range of vertical velocities giving maximum correlation in (b). (b) Correlation coefficients between basal return amplitude and accretion time series calculated for a range of non-melt vertical displacement rates, dashed lines mark the maximum correlation: (purple) correlation of the full time series, (green) correlation of time series reduced to 0 (no accretion, no amplitude decrease) and 1 (accretion, amplitude decrease).

zones and above channels we generally expect ice shelf to bend and have its strain rate be a linear function of depth (Jenkins et al., 2006), while away from these zones we expect hydrostatic balance and a depth-independent strain rate, however, more complicated strain rate profiles are possible. Here we show how the validity of a vertical strain rate estimate can be assessed independently in a situation where intermittent accretion occurs.

Site 5a is an example of a location where the presence of off-nadir internal reflectors and weak internal reflectors at depth can cause uncertainties in vertical strain rate estimates (Figure 13a). There are two sets of off-nadir reflectors; one near 100 m range and the other between 200 and 400 m range. Further, at ranges greater than ~500 m the internal reflections become weak and their displacements dominated by noise. Assuming Site 5a is freely floating, which implies a depth-independent vertical strain rate, a line is fitted to the time-mean displacements of internal reflectors. Fitting generally excludes reflectors that are off-nadir, noisier than a certain threshold, or affected by firn compaction, because these could corrupt the strain rate estimation. The intersection of line fit with the location of the ice base constitutes basal displacements from all processes other than melting (Nicholls et al., 2015). While the line fit appears to be appropriate for Site 5a, it relies on a relatively small number of data points because over half of the range had to be excluded from fitting. Therefore, having a complimentary estimate of the ice dynamical contribution to thinning would increase confidence in the result.

An independent way to accurately determine the non-melt basal displacement makes use of intermittent accretion episodes. During an accreted-ice event, marine-ice presence is detectable in both the return

amplitude and the accreted thickness time series as anomalies that occur at the same time. If an incorrect mean non-melt basal displacement were subtracted from the time series of thickness rate of change, the resulting melt rate time series would have a constant offset. When integrated, the calculated duration of accreted-ice events would be distorted and the match with anomalies in the return amplitude time series would be poor. Therefore, to estimate the non-melt basal displacement we consider all the possibilities: we calculate the respective melt rates and accretion thickness time series, and choose the one where accretion and the drops in the return amplitude time series show the best match. This can be assessed by calculating the correlation coefficient between the detrended return amplitude time series and each accreted thickness time series. Alternatively, we can also calculate the percentage of data points that have either accreted ice and reduced amplitude, or no apparent accretion and no amplitude reduction. The mean melt rate for which there is a maximum agreement between amplitude drop and apparent accretion is the most likely to be correct (Figure 13b). At Site 5a the two independent estimates agree within the error estimate, which increases confidence in the mean melt rate derived using a depth-independent vertical strain rate. The same occurs at R02, where the number of good internal reflectors is also limited (Figure 13a).

7.2. Melt Rate Estimation From Infrequent Measurements

Average basal melt rates are often measured from repeat visits by cross-correlating two ApRES shots typically separated by a year (Stewart et al., 2019). However, if a surveyed site is located in a regime of intermittent accretion, this can impact the accuracy of the estimate even if the cross-correlation analysis indicates that the site has melted. To determine the melt rate with accuracy greater than the range resolution, it is necessary to test the robustness of the phase-dependent contribution to the melt rate by analyzing the signal over a range of different center frequencies. If the resulting melt rate is frequency-dependent, it could indicate that ice was accreted at the base during at least one of the two measurements. At sites where either long-term or intermittent accretion is suspected to occur, the inferred accretion rates should be interpreted with caution, because both the dielectric constant and electrical conductivity of accreted ice differ from those of glacial ice. As we have shown (e.g., Figure 8), both quantities can contribute to the measured thickness change; the dielectric constant sets the speed of wave propagation through the material and, together with the electrical conductivity, modifies the phase of the reflected signal.

8. Summary and Conclusions

Autonomously sampling ApRES at three sites at the Ronne Ice Shelf showed signatures of intermittent basal accretion. We observed that, when ice accretes at the base, the basal reflection changes its phase and amplitude and that this change is different for different transmit frequencies. This led us to conclude that phase changes during apparent basal accretion cannot be directly interpreted as changes in thickness and that the lack of knowledge of the electromagnetic properties of the accreted ice limits precise measurements of changes in ice thickness for the time the accreted ice is present.

To estimate the dielectric constant, electrical conductivity, and thickness of the accreted ice simultaneously, we used a three-layer model that computes how a reflection from an ice base changes when a third, marine-ice layer is introduced between glacial ice base and ISW. A comparison of the model output with the ApRES observations resulted in a set of possible combinations of the accreted ice properties. The most likely solutions at one site (R02) yielded a dielectric constant of 32–46, the electrical conductivity of 0.6–1 S/m, and the mean accretion rate during the initial buildup equivalent to 1–3 mm/day of glacial ice. The high values of electromagnetic properties and high accretion rates imply that precipitation of frazil ice crystallized from supercooled water must be the dominant mechanism responsible for the observed ice formation at this site. These results rely on a mixing model assumption, and we do not have concurrent direct measurements that would provide an independent estimate of the accretion rates and properties.

We were unable to constrain the accreted-ice properties at two other sites (R03 and Site 5a) and attributed this failure to the effect of basal roughness. The analysis was complicated by observed non-monotonic frequency-dependent changes in the reflected signal. Within the framework of the three-layer model, this observation requires an introduction of a frequency-dependent roughness parameter, making the problem poorly constrained. However, even if we cannot constrain the accretion rates at these sites, we are still able

to reliably detect accreted-ice events from anomalies in the basal echo. This is useful, as even a simple detection of the frequency and duration of accreted-ice events and temporal evolution of these statistics can provide valuable information on oceanographic changes in the ice-shelf cavity.

We have shown that it is possible to detect and quantify episodic accretion at a melting ice-shelf base using a phase-sensitive radar. Observations from the western portion of the Ronne Ice Shelf indicate that basal accretion is caused primarily by the deposition of frazil ice crystals sourced from lateral displacements of potentially supercooled water at a variety of time scales, each associated with a different process. Our findings show how the ability to reliably detect episodic basal accretion events opens the possibility to monitor and infer ocean dynamical processes in the sub-ice-shelf ocean using remote observations.

Data Availability Statement

The ApRES data are available at https://doi.org/10.6084/m9.figshare.14049410.

Acknowledgments
This project has received funding from the European Union's Horizon 2020 research and innovation programme under the Marie Skłodowska-Curie grant agreement No 790062. The ApRES data were collected as part of the NERC-funded project NE/L013770/1: Ice shelves in a warming world: Filchner Ice Shelf System (FISS), Antarctica. The authors thank Craig Stewart, one anonymous reviewer, and Laurie Padman for their constructive feedback.

References

Beckmann, P., & Spizzichino, A. (1963). *The scattering of electromagnetic waves from rough surfaces*: MacMillan. 1963.
Brennan, P. V., Lok, L. B., Nicholls, K., & Corr, H. (2014). Phase-sensitive FMCW radar system for high-precision Antarctic ice shelf profile monitoring. *Sonar Navigation IET Radar*, *8*(7), 776–786. https://doi.org/10.1049/iet-rsn.2013.0053
Corr, H. F., Jenkins, A., Nicholls, K. W., & Doake, C. S. M. (2002). Precise measurement of changes in ice-shelf thickness by phase-sensitive radar to determine basal melt rates. *Geophysical Research Letters*, *29*(8), 73–81. https://doi.org/10.1029/2001GL014618
Craven, M., Allison, I., Fricker, H. A., & Warner, R. (2009). Properties of a marine ice layer under the Amery Ice Shelf, East Antarctica. *Journal of Glaciology*, *55*(192), 717–728. https://doi.org/10.3189/002214309789470941
Craven, M., Warner, R., Galton-Fenzi, B., Herraiz-Borreguero, L., Vogel, S., & Allison, I. (2014). Platelet ice attachment to instrument strings beneath the Amery Ice Shelf, East Antarctica. *Journal of Glaciology*, *60*(220), 383–393. https://doi.org/10.3189/2014JoG13J082
Foldvik, A., Gammelsrød, T., & Tørresen, T. (1985). Circulation and water masses on the Southern Weddell sea shelf. *In Oceanology of the Antarctic continental shelf* (pp. 5–20). American Geophysical Union (AGU). https://doi.org/10.1029/AR043p0005
Gammelsrød, T., Foldvik, A., Nøst, O. A., Foldvik, Ø., Anderson, L. G., Fogelqvist, E., et al. (1994). Distribution of water masses on the continental shelf in the Southern Weddell Sea. *In The polar oceans and their role in shaping the global environment* (pp. 159–176). American Geophysical Union (AGU). https://doi.org/10.1029/GM085p0159
Hashin, Z., & Shtrikman, S. (1962). A variational approach to the theory of the effective magnetic permeability of multiphase materials. *Journal of Applied Physics*, *33*(10), 3125–3131. https://doi.org/10.1063/1.1728579
Holland, D. M., & Jenkins, A. (1999). Modeling thermodynamic ice–ocean interactions at the base of an ice shelf. *Journal of Physical Oceanography*, *29*(8), 1787–1800. https://doi.org/10.1175/1520-0485(1999)029<1787:mtioia>2.0.co;2
Jenkins, A., Corr, H. F. J., Nicholls, K. W., Stewart, C. L., & Doake, C. S. M. (2006). Interactions between ice and ocean observed with phase-sensitive radar near an Antarctic ice-shelf grounding line. *Journal of Glaciology*, *52*(178), 325–346. https://doi.org/10.3189/172756506781828502
Lambrecht, A., Sandhäger, H., Vaughan, D. G., & Mayer, C. (2007). New ice thickness maps of Filchner–Ronne Ice Shelf, Antarctica, with specific focus on grounding lines and marine ice. *Antarctic Science*, *19*(4), 521–532. https://doi.org/10.1017/S0954102007000661
Lewis, E. L., & Perkin, R. G. (1986). Ice pumps and their rates. *Journal of Geophysical Research: Oceans*, *91*(C10), 11756–11762. https://doi.org/10.1029/JC091iC10p11756
Looyenga, H. (1965). Dielectric constants of heterogeneous mixtures. *Physica*, *31*(3), 401–406. https://doi.org/10.1016/0031-8914(65)90045-5
Morey, R. M., & Kovacs, A. (1982). *The effects of conductivity on high-resolution Impulse radar sounding, Ross ice shelf, Antarctica*. (Tech. Rep. No. 82-42). U.S. Army Cold Regions Research and Engineering Laboratory.
Morey, R. M., Kovacs, A., & Cox, G. F. N. (1984). Electromagnetic properties of sea ice. *Cold Regions Science and Technology*, *9*(1), 53–75. https://doi.org/10.1016/0165-232X(84)90048-X
Morlighem, M., Rignot, E., Binder, T., Blankenship, D., Drews, R., Eagles, G., et al. (2020). Deep glacial troughs and stabilizing ridges unveiled beneath the margins of the Antarctic ice sheet. *Nature Geoscience*, *13*(2), 132–137. https://doi.org/10.1038/s41561-019-0510-8
Neal, C. S. (1979). The dynamics of the Ross Ice Shelf revealed by radio echo-sounding. *Journal of Glaciology*, *24*(90), 295–307. https://doi.org/10.3189/S0022143000014817
Nicholls, K. W. (1996). Temperature variability beneath Ronne Ice Shelf, Antarctica, from thermistor cables. *Journal of Geophysical Research: Oceans*, *101*(C1), 1199–1210. https://doi.org/10.1029/95JC02679
Nicholls, K. W. (2018). The study of ice shelf-ocean interaction—Techniques and recent results. *Advances in Polar Science*, *29*(3), 9.
Nicholls, K. W., Corr, H. F., Stewart, C. L., Lok, L. B., Brennan, P. V., & Vaughan, D. G. (2015). A ground-based radar for measuring vertical strain rates and time-varying basal melt rates in ice sheets and shelves. *Journal of Glaciology*, *61*(230), 1079–1087. https://doi.org/10.3189/2015JoG15J073
Nicholls, K. W., Makinson, K., & Johnson, M. R. (1997). New oceanographic data from beneath Ronne Ice Shelf, Antarctica. *Geophysical Research Letters*, *24*(2), 167–170. https://doi.org/10.1029/96GL03922
Nicholls, K. W., Makinson, K., & Robinson, A. V. (1991). Ocean circulation beneath the Ronne ice shelf. *Nature*, *354*(6350), 221–223. https://doi.org/10.1038/354221a0
Nicholls, K. W., Østerhus, S., Makinson, K., & Johnson, M. R. (2001). Oceanographic conditions south of Berkner Island, beneath Filchner-Ronne Ice Shelf, Antarctica. *Journal of Geophysical Research: Oceans*, *106*(C6), 11481–11492. https://doi.org/10.1029/2000JC000350
Nicholls, K. W., Padman, L., Schröder, M., Woodgate, R. A., Jenkins, A., & Østerhus, S. (2003). Water mass modification over the continental shelf north of Ronne Ice Shelf, Antarctica. *Journal of Geophysical Research: Oceans*, *108*(C8), 3260. https://doi.org/10.1029/2002JC001713
Oerter, H., Kipfstuhl, J., Determann, J., Miller, H., Wagenbach, D., Minikin, A., & Graft, W. (1992). Evidence for basal marine ice in the Filchner–Ronne ice shelf. *Nature*, *358*(6385), 399–401. https://doi.org/10.1038/358399a0

Orfanidis, S. J. (2002). *Electromagnetic waves and antennas*. ECE Department.
Robin, G. D. Q., Doake, C. S. M., Kohnen, H., Crabtree, R. D., Jordan, S. R., & Möller, D. (1983). Regime of the Filchner–Ronne ice shelves, Antarctica. *Nature*, *302*(5909), 582–586. https://doi.org/10.1038/302582a0
Robin, G. D. Q., Evans, S., Bailey, J. T., & Bullard, E. C. (1969). Interpretation of radio echo sounding in polar ice sheets. *Philosophical Transactions of the Royal Society of London*, *265*(1166), 437–505. https://doi.org/10.1098/rsta.1969.0063
Robinson, A., Makinson, K., & Nicholls, K. (1994). The oceanic environment beneath the northwest Ronne Ice Shelf, Antarctica. *Annals of Glaciology*, *20*, 386–390. https://doi.org/10.3189/1994AoG20-1-386-390
Robinson, N. J., Grant, B. S., Stevens, C. L., Stewart, C. L., & Williams, M. J. M. (2020). Oceanographic observations in supercooled water: Protocols for mitigation of measurement errors in profiling and moored sampling. *Cold Regions Science and Technology*, *170*, 102954. https://doi.org/10.1016/j.coldregions.2019.102954
Stevens, C., Hulbe, C., Brewer, M., Stewart, C., Robinson, N., Ohneiser, C., & Jendersie, S. (2020). Ocean mixing and heat transport processes observed under the Ross Ice Shelf control its basal melting. *Proceedings of the National Academy of Sciences*, *117*, 16799–16804. https://doi.org/10.1073/pnas.1910760117
Stewart, C. L. (2018). *Ice-ocean interactions beneath the north-western Ross ice shelf, Antarctica*. Thesis, University of Cambridge. https://doi.org/10.17863/CAM.21483
Stewart, C. L., Christoffersen, P., Nicholls, K. W., Williams, M. J. M., & Dowdeswell, J. A. (2019). Basal melting of Ross Ice Shelf from solar heat absorption in an ice-front polynya. *Nature Geoscience*, *12*(6), 435–440. https://doi.org/10.1038/s41561-019-0356-0
Thyssen, F. (1988). Special aspects of the central part of Filchner-Ronne Ice Shelf, Antarctica. *Annals of Glaciology*, *11*, 173–179. https://doi.org/10.3189/S0260305500006509
Vaňková, I., Cook, S., Winberry, J. P., Nicholls, K. W., & Galton-Fenzi, B. K. (2021). Deriving melt rates at a complex ice shelf base using in situ radar: Application to totten ice shelf. *Geophysical Research Letters*, *48*(7). https://doi.org/10.1029/2021GL092692
Vaňková, I., Nicholls, K. W., Corr, H. F. J., Makinson, K., & Brennan, P. V. (2020a). Observations of tidal melt and vertical strain at the Filchner-Ronne Ice Shelf, Antarctica. *Journal of Geophysical Research: Earth Surface*, *125*(1). https://doi.org/10.1029/2019JF005280
Vaňková, I., Nicholls, K. W., Xie, S., Parizek, B. R., Voytenko, D., & Holland, D. M. (2020b). Depth-dependent artifacts resulting from ApRES signal clipping. *Annals of Glaciology*, *61*(81), 108–113. https://doi.org/10.1017/aog.2020.56
Weeks, W. F., & Ackley, S. F. (1982). *The growth, structure, and properties of sea ice (Tech. Rep. No. 82-1)*. U.S. Army Cold Regions Research and Engineering Laboratory.
Zotikov, I. A., Zagorodnov, V. S., & Raikovsky, J. V. (1980). Core drilling through the Ross Ice Shelf (Antarctica) confirmed basal freezing. *Science*, *207*(4438), 1463–1465. https://doi.org/10.1126/science.207.4438.1463